

LETTER TO THE EDITOR

Discovery of two isomers of ethynyl cyclopentadiene in TMC-1: Abundances of CCH and CN derivatives of hydrocarbon cycles[★]

J. Cernicharo¹, M. Agúndez¹, R. I. Kaiser², C. Cabezas¹, B. Tercero^{3,4}, N. Marcelino⁴, J. R. Pardo¹, and P. de Vicente³

¹ Grupo de Astrofísica Molecular, Instituto de Física Fundamental (IFF-CSIC), C/ Serrano 121, 28006 Madrid, Spain
e-mail: jose.cernicharo@csic.es

² Department of Chemistry, University of Hawaii at Manoa, Honolulu, HI 96822, USA

³ Centro de Desarrollos Tecnológicos, Observatorio de Yebes (IGN), 19141 Yebes, Guadalajara, Spain

⁴ Observatorio Astronómico Nacional (OAN, IGN), Madrid, Spain

Received; accepted

ABSTRACT

We report the detection of two isomers of ethynyl cyclopentadiene (*c*-C₅H₅CCH), namely 1- and 2-ethynyl-1,3-cyclopentadiene, in the direction of TMC-1. We derive column densities of $(1.4\pm 0.2)\times 10^{12}$ cm⁻² and $(2.0\pm 0.4)\times 10^{12}$ cm⁻², respectively, for these two cyclopentadiene derivatives, which imply that they are about ten times less abundant than cyclopentadiene. We also report the tentative detection of ethynyl benzene (C₆H₅CCH), for which we estimate a column density of $(2.5\pm 0.4)\times 10^{12}$ cm⁻². We derived abundances for the corresponding cyano derivatives of cyclopentadiene and benzene and found values significantly lower than previously reported. The rotational temperature of the ethynyl and cyano derivatives of these cycles is about 9 K, that is, very close to the gas kinetic temperature of the cloud. The abundance ratio of the 1- and 2- isomers of ethynyl cyclopentadiene is 1.4 ± 0.5 , while for the two isomers of cyano cyclopentadiene it is 2.4 ± 0.6 . The relative abundances of CCH over CN derivatives is 7.7 ± 2.2 for cyclopentadiene, which probably reflects the abundance ratio of the radicals CCH and CN; this ratio is only 2.1 ± 0.5 for benzene, which suggests that additional reactions besides cyano radicals with benzene are involved in the formation of benzonitrile. The formation of these cycles is reasonably well accounted for through a chemical scheme based on neutral-neutral reactions. It is predicted that benzene should be as abundant as cyclopentadiene in TMC-1.

Key words. molecular data – line: identification – ISM: molecules – ISM: individual (TMC-1) – astrochemistry

1. Introduction

The QUIJOTE¹ (Cernicharo et al., 2021a) and the GOTHAM² (McGuire et al., 2018) line surveys are providing exciting results of the abundance of hydrocarbons and their ethynyl and cyano derivatives in the cold pre-stellar core Taurus Molecular Cloud 1 (TMC-1). Species such as the propargyl radical (CH₂CCH), vinylacetylene (CH₂CHCCH), ethynylallene (H₂CCCHCCH), and cyclic hydrocarbons such as cyclopentadiene (*c*-C₅H₆), *o*-benzyne (C₆H₄), and indene (*c*-C₉H₈) (Agúndez et al., 2021a; Cernicharo et al., 2021a,b,c,d) have been detected using the QUIJOTE line survey through a line-by-line identification process. Using spectral stacking techniques, the GOTHAM line survey has provided the detections of the cyano derivatives of cyclopentadiene, benzene, and naphthalene (McGuire et al., 2021; Lee et al., 2021; McGuire et al., 2018). These results reveal a new and unexpected chemistry that requires a profound revision of the chemical processes at work in cold dark clouds such as TMC-1. In order to provide an adequate reference for chemical models, reliable molecular abundances need to be obtained. Moreover, observing distinct ethynyl and cyano derivatives of

hydrocarbons can provide important constraints on the reactivity of CCH and CN radicals with unsaturated acyclic and cyclic hydrocarbons.

In this letter we report the discovery of two isomers of ethynyl cyclopentadiene (*c*-C₅H₅CCH) and the tentative detection of ethynyl benzene (C₆H₅CCH, hereinafter referred to as *EBZ*) towards TMC-1. From our data we also derive column densities for the corresponding cyano derivatives of benzene and cyclopentadiene, previously detected by McGuire et al. (2018), McCarthy et al. (2021), and Lee et al. (2021), providing a rigorous confirmation of the presence of these species in TMC-1 based on a line-by-line detection procedure and a coherent and homogeneous set of abundances for the CCH and CN derivatives of cyclopentadiene and benzene.

2. Observations

New receivers, built within the Nanocosmos project³ and installed at the Yebes 40m radio telescope, were used for the observations of TMC-1 ($\alpha_{J2000} = 4^{\text{h}}41^{\text{m}}41.9^{\text{s}}$ and $\delta_{J2000} = +25^{\circ}41'27.0''$). A detailed description of the system is given by Tercero et al. (2021). The receiver consists of two cold high electron mobility transistor amplifiers that cover the 31.0-50.3 GHz band with horizontal and vertical polarizations. Receiver temperatures in the runs conducted in 2020 vary from 22 K at 32 GHz to 42 K at 50 GHz. Some power adaptation in the down-conversion

[★] Based on observations carried out with the Yebes 40m telescope (projects 19A003, 20A014, 20D023, and 21A011). The 40m radio telescope at Yebes Observatory is operated by the Spanish Geographic Institute (IGN, Ministerio de Transportes, Movilidad y Agenda Urbana).

¹ Q-band Ultrasensitive Inspection Journey to the Obscure TMC-1 Environment

² GBT Observations of TMC-1: Hunting Aromatic Molecules

³ <https://nanocosmos.iff.csic.es/>

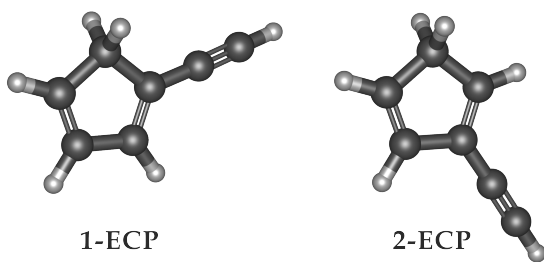


Fig. 1. Scheme of the two lowest energy isomers of ethynyl cyclopentadiene.

chains have reduced the receiver temperatures in 2021 to 16 K at 32 GHz and 30 K at 50 GHz. The backends are $2 \times 8 \times 2.5$ GHz fast Fourier transform spectrometers with a spectral resolution of 38.15 kHz, providing the whole coverage of the Q band in both polarizations. All observations were performed in the frequency switching mode with frequency throws of 8 and 10 MHz. The main beam efficiency varies from 0.6 at 32 GHz to 0.43 at 50 GHz. Pointing corrections were derived from nearby quasars and SiO masers, and errors were always within 2-3". The telescope beam size is 56" and 31" at 31 and 50 GHz, respectively. The intensity scale used in this work, antenna temperature (T_A^*), was calibrated using two absorbers at different temperatures and the atmospheric transmission model ATM (Cernicharo, 1985; Pardo et al., 2001). Calibration uncertainties were adopted to be 10 %. All data were analysed using the GILDAS package⁴. Details of the QUIJOTE line survey are provided by Cernicharo et al. (2021d). The 1σ sensitivity of the survey varies between 0.17 and 0.30 mK between 31 and 50 GHz.

3. Detection of cycles in TMC-1

Line identification in this work was done using the catalogues MADEX (Cernicharo, 2012), CDMS (Müller et al., 2005), and JPL (Pickett et al., 1998). By September 2021, the MADEX code contained 6377 spectral entries corresponding to the ground and vibrationally excited states, together with the corresponding isotopologues, of 1696 molecules.

The recent detection of cyclopentadiene (Cernicharo et al., 2021a) and of its cyano derivatives (McCarthy et al., 2021; Lee et al., 2021) suggests that other derivatives of cyclopentadiene could be present in this source, in particular the ethynyl ones, 1- and 2-ethynyl-1,3-cyclopentadiene (hereinafter referred to as 1-*ECP* and 2-*ECP*, respectively; see Fig. 1). These two isomers of ethynyl cyclopentadiene were observed in the laboratory by McCarthy et al. (2020). We used these data to fit the rotational and distortion constants in order to predict the frequencies of their rotational transitions within the Q band (see Sects. 3.1.1 and 3.1.2). The calculated uncertainties for these transitions are 10-25 kHz (0.1-0.3 km s⁻¹).

3.1. The isomers of ethynyl cyclopentadiene

The substitution of a hydrogen atom by an ethynyl (CCH) group in cyclopentadiene (*c*-C₅H₆) yields three possible isomers of ethynyl cyclopentadiene. Quantum chemical calculations at the MP2/6-311++G(d,p) level of theory (Møller & Plesset, 1934; Frisch et al., 1984) predict 1-*ECP* as the most stable isomer, followed closely by 2-*ECP* (6 kJ mol⁻¹) and then 5-ethynyl-1,3-cyclopentadiene, whose energy is far higher (by 27 kJ mol⁻¹).

⁴ <http://www.iram.fr/IRAMFR/GILDAS>

The structures of the two isomers 1-*ECP* and 2-*ECP* are shown in Fig. 1. The two isomers are moderately polar, with dipole moments along their *a*- and *b*-inertial axes. The predicted μ_a values for 1-*ECP* and 2-*ECP* are 0.81 and 1.11 D, respectively, while the μ_b values are 0.32 and 0.37 D, respectively, in good agreement with previous calculations (Lee & McCarthy, 2019). Both isomers were observed in the laboratory by McCarthy et al. (2020) (we note that 2-*ECP* was named 5-ethynyl-1,3-cyclopentadiene in their work). The low value of μ_b for the two isomers results in *b*-type transitions that are around ten times weaker than the *a*-type ones. In the following, we start our search with the isomer with the largest dipole moment, namely 2-*ECP*.

3.1.1. Detection of 2-ethynyl-1,3-cyclopentadiene (2-*ECP*)

The laboratory data for 2-*ECP*, the isomer with the largest dipole moment along the *a* axis, cover the frequency range 6.5-25.8 GHz with $J_{max}=8$ (McCarthy et al., 2020). McCarthy et al. (2020) quote an uncertainty on their frequencies of 2 kHz. However, their own fit provides a standard deviation of 4.5 kHz. We thus assigned an uncertainty of 4 kHz to all their measured frequencies, except for the $7_{1,6}-6_{1,5}$ line, for which they quote an uncertainty of 10 kHz. The resulting rotational and distortion constants with the new uncertainties do not show a significant variation with respect to their constants. However, the standard deviation of the fit improves to 3 kHz if the distortion constant δ_J is also included in the fit (see Table A.3). This new set of constants was used to predict the frequencies of the rotational lines of 2-*ECP* in the 31-50 GHz domain.

A total of 24 *a*-type lines of 2-*ECP* were detected in TMC-1 above the 3σ level with the QUIJOTE line survey. Some of them are shown in Fig. 2. The derived line parameters are given in Appendix A (see Table A.1). A fit to the observed line profiles assuming a source diameter of 80" (Fossé et al., 2001) provides a rotational temperature of 9.0 ± 1.0 K and a column density of $(1.4 \pm 0.2) \times 10^{12}$ cm⁻². The synthetic spectra are compared with observations in Fig. 2 (red line). With the adopted source diameter, the molecular emission fills the main beam of the telescope at all observed frequencies.

All observed lines of 2-*ECP* correspond to values of *J* between 9-14 and $K_a \leq 3$; hence, the associated upper level energies cover the range 8-20 K. Rotational temperatures below 8 K underestimate the emission of the transitions arising from the higher energy levels. Nevertheless, transitions involving energy levels between 8 and 12 K are not very sensitive to the rotational temperature and can be fitted with rotational temperatures as low as 6 K with a modest variation in the column density. This effect is discussed in detail in Appendix A of Cernicharo et al. (2021e). A similar situation has been found for the cyano derivatives of cyclopentadiene and benzene (see our Appendices B and C), which have considerably larger dipole moments. The near thermalization of the rotational levels of the derivatives of cyclopentadiene and benzene is most likely due the large collisional rates we could expect for these molecules, which exhibit a much larger geometrical cross-section than linear molecules such as HC₅N and HC₇N, for which rotational temperatures around 8-9 K have also been found (Cernicharo et al., 2020). A similar rotational temperature of ~ 9 K has been derived for indene and cyclopentadiene (Cernicharo et al., 2021a).

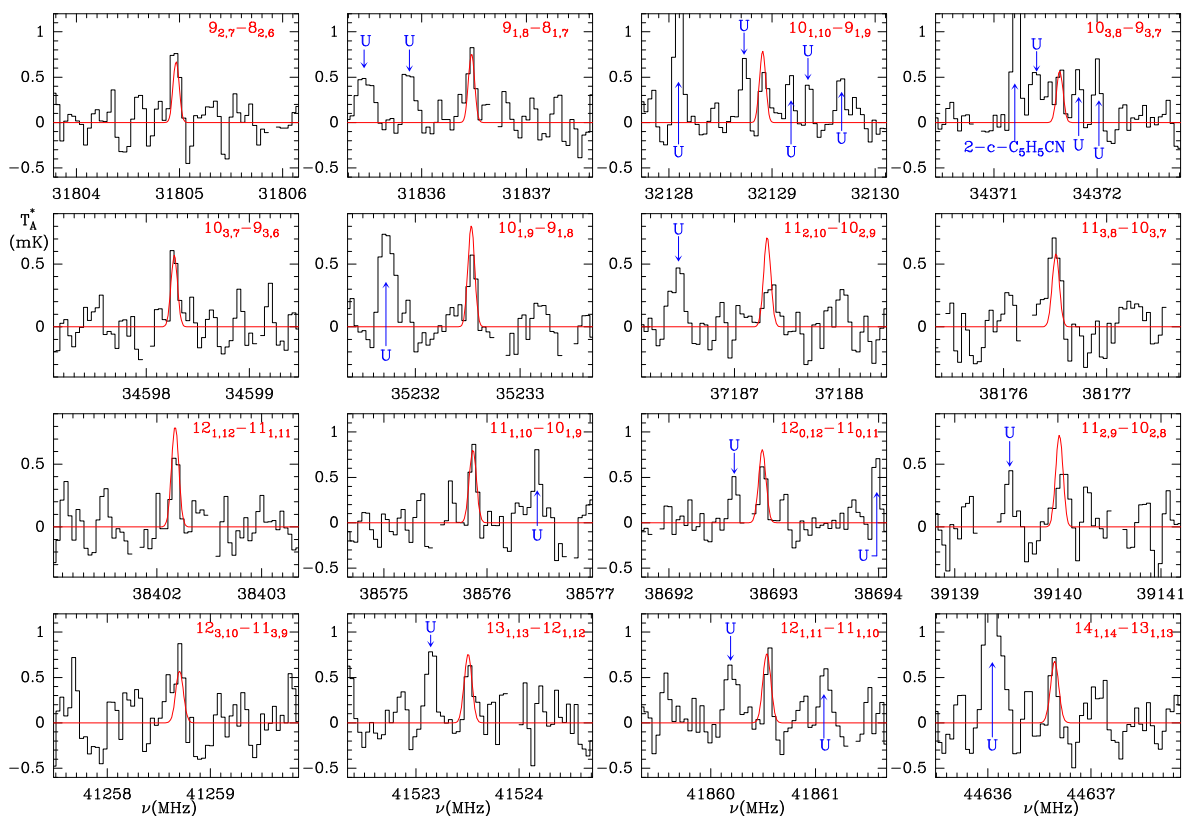


Fig. 2. Subset of the observed lines of 2-*ECP* in the 31–50 GHz frequency range towards TMC-1. Line parameters for the complete list of detected lines of 2-*ECP* are given in Table A.1. The abscissa corresponds to the rest frequency assuming a local standard of rest velocity of 5.83 km s⁻¹. The ordinate is the antenna temperature corrected for atmospheric and telescope losses in mK. The red line shows the synthetic spectrum obtained from a fit to the observed line profiles, which provides $T_r = 9 \pm 1$ K and $N(2\text{-}ECP) = (1.4 \pm 0.2) \times 10^{12}$ cm⁻². The rotational quantum numbers are indicated in each panel. Blanked channels correspond to negative features produced in the folding of the frequency switching data.

3.1.2. Detection of 1-ethynyl-1,3-cyclopentadiene (1-*ECP*)

The laboratory data for 1-*ECP* (McCarthy et al., 2020) cover the frequency range 6.5–24.9 GHz with $J_{max} = 7$ and $K_a \leq 3$. McCarthy et al. (2020) quote a standard deviation for their fit of 2.7 kHz. However, it is possible to reduce this value to 1.1 kHz by fitting the distortion constant δ_K . The new rotational and distortion constants, which are given in Table A.3, were used to predict the frequencies of the rotational lines of 1-*ECP* in the 31–50 GHz domain.

If the abundances of the two isomers were identical, the a -type lines of 1-*ECP* would be 1.9 times weaker than those of 2-*ECP* (the squared ratio of the a component of the dipole moment). Hence, we expect to detect only the strongest transitions of 1-*ECP*. A total of 14 lines of 1-*ECP* were detected in TMC-1 above the 3σ level with the current sensitivity of the QUIJOTE line survey. Some of them are shown in Fig. A.1. The derived line parameters are given in Appendix A (see Table A.2). A fit to the observed line profiles assuming the same source size (80'') and rotational temperature (9 K) as for 2-*ECP* provides a column density of $(2.0 \pm 0.4) \times 10^{12}$ cm⁻². Therefore, the isomer 2-*ECP* is a factor of 1.4 ± 0.5 more abundant than 1-*ECP*.

The detection of the two isomers of ethynyl cyclopentadiene is robust since it is based on the detection of a significant number of individual transitions. Taking into account the column density of $(1.2 \pm 0.3) \times 10^{13}$ cm⁻² derived for cyclopentadiene (Cernicharo et al., 2021a), 1-*ECP* and 2-*ECP* are less abundant than cyclopentadiene by factors of 6.0 ± 2.5 and 8.6 ± 3.3 , respectively.

Finally, improved molecular constants for 1-*ECP* and 2-*ECP* resulting from a merged fit to the laboratory data and the

observed frequencies in TMC-1 are provided in Appendix A.1 (see Table A.3).

3.2. Ethynyl benzene

Laboratory spectroscopy for *EBZ*, C₆H₅CCH, has been provided by different authors covering frequencies up to 340 GHz, J up to 140, and K_a up to 48 (Cox et al., 1975; Dreizler et al., 2004; Kisiel & Krańnicki, 2010). Hence, the frequency predictions in the range of our line survey are rather accurate, with calculated uncertainties below 1 kHz. The dipole moment of the molecule is low, 0.66 D (Cox et al., 1975). Hence, we could expect weak emission lines in our data. The molecule has two pairs of identical hydrogen nuclei, which introduces an *ortho* and *para* spin statistic. *Ortho* and *para* levels correspond to K_a even and odd, respectively. The ratio of statistical weights is 5/3. The lowest energy *para* level (1_{1,1}) is 0.33 K above the ground *ortho* level (0_{0,0}). Due to the low dipole moment and the ~ 1.7 factor in the statistical weights, we do not expect to have enough sensitivity in our data to detect the *para* transitions. A quick examination of all $K_a = 0$ and 2 lines reveals only four lines at the 3σ limit of the survey. All explored lines are summarized in Appendix A.2 (see Table A.6). The four detected lines are shown in Fig. A.2. With this limited number of lines, it is not possible to claim a detection. Tentatively, we derive a column density of $(2.5 \pm 0.4) \times 10^{12}$ cm⁻² for an assumed rotational temperature of 9 K and a source size of 80''. Taking into account the density of unknown features, we consider that a stacking of our data is hazardous and that a definitive detection has to wait for the improvement of the QUI-

JOTE line survey. Assuming that the derived column density is a 3σ limit, the relative abundance of ethynyl cyclopentadiene (the two isomers) and *EBZ* is ≥ 1.4 , which suggests that their potential cyclopentadiene and benzene precursors have abundances of the same order in TMC-1.

3.3. Cyano derivatives of cyclopentadiene and benzene

Two cyano derivatives of cyclopentadiene (hereinafter referred to as 1-*CCP* and 2-*CCP*; see Appendix B) were detected in TMC-1 using stacking techniques by McCarthy et al. (2021) and Lee et al. (2021). A few individual lines of 1-*CCP* were reported by Lee et al. (2021). There are some discrepancies between the column densities reported by these authors for 1-*CCP*. McCarthy et al. (2021) derive $N(1\text{-}CCP) = (1.44 \pm 0.17) \times 10^{12} \text{ cm}^{-2}$ and $T_{rot} = 6.0 \pm 0.3 \text{ K}$, while Lee et al. (2021) find a column density of $(8.3 \pm 0.1) \times 10^{11} \text{ cm}^{-2}$ and a rotational temperature of $6.00 \pm 0.03 \text{ K}$. For 2-*CCP*, Lee et al. (2021) derive a column density of $1.9 \times 10^{11} \text{ cm}^{-2}$. In order to provide a coherent and homogeneous set of column densities, we analyse the lines of the two isomers in Appendix B. The observed lines of 1-*CCP* are shown in Fig. B.1 and those of 2-*CCP* in Fig. B.2. Line parameters for the two species are given in Tables B.1 and B.2, respectively. We derive a rotational temperature of $9.0 \pm 1.0 \text{ K}$ for both species and column densities of $(3.1 \pm 0.3) \times 10^{11} \text{ cm}^{-2}$ and $(1.3 \pm 0.2) \times 10^{11} \text{ cm}^{-2}$ for 1-*CCP* and 2-*CCP*, respectively. The isomer 1-*CCP* is 2.4 times more abundant than 2-*CCP*, which is twice lower than the abundance ratio found by Lee et al. (2021). The discrepancies with previous works are discussed in Appendix B.

Benzonitrile, C_6H_5CN , was previously detected towards TMC-1 by McGuire et al. (2018) through stacking techniques and some well-detected individual lines. They obtain a rotational temperature of 7 K and a column density of $4 \times 10^{11} \text{ cm}^{-2}$. In a more recent work, Burkhardt et al. (2021) derive a column density of $1.6 \times 10^{12} \text{ cm}^{-2}$ (i.e. a factor of four higher than previously reported) and a rotational temperature of $6.1 \pm 0.3 \text{ K}$. In Appendix C we discuss the 100 individual lines of this species detected with high sensitivity with QUIJOTE's data. They are shown in Figs. C.1, C.2, C.3, and C.4. We obtain a rotational temperature of $9.0 \pm 0.5 \text{ K}$ and a total column density of $(1.2 \pm 0.1) \times 10^{12} \text{ cm}^{-2}$. A rotational temperature of 6 K cannot explain the observed emission of lines with $K_a \geq 4$ (see the caption of Fig. C.1 and Appendix C).

All column densities derived in this work are summarized in Table 1.

4. Chemistry of cycles in TMC-1

It is remarkable that, given their chemical complexity, the CCH and CN derivatives of cyclopentadiene and benzene are observed with relatively large abundances in TMC-1. To understand how these species can be formed, we built a chemical model similar to that used in previous recent studies of TMC-1 (e.g. Cernicharo et al. 2021d). Briefly, we adopted typical conditions of cold dark clouds – namely, a gas temperature of 10 K, a volume density of H nuclei of $2 \times 10^4 \text{ cm}^{-3}$, a cosmic-ray ionization rate of H_2 of $1.3 \times 10^{-17} \text{ s}^{-1}$, a visual extinction of 30 mag, and the so-called low-metal elemental abundances (e.g. Agúndez & Wakelam 2013) – with the exception of oxygen, for which we decreased the abundance (see below). The core of the chemical network is the RATE12 network of the UMIST database (McElroy et al., 2013), with updates from Loison et al. (2015), Marcelino et al. (2021), Agúndez et al. (2021a,b), and Cernicharo et al.

Table 1. Abundances of ethynyl and cyano species in TMC-1.

Molecule	N (cm^{-2})	Abundance ^a	Comments
<i>c</i> -C ₅ H ₆	1.3×10^{13}	1.3×10^{-09}	1
1- <i>c</i> -C ₅ H ₅ CCH	1.4×10^{12}	1.4×10^{-10}	2
2- <i>c</i> -C ₅ H ₅ CCH	2.0×10^{12}	2.0×10^{-10}	2
1- <i>c</i> -C ₅ H ₅ CN	3.1×10^{11}	3.1×10^{-11}	2,A
2- <i>c</i> -C ₅ H ₅ CN	1.3×10^{11}	1.3×10^{-11}	2,B
C ₆ H ₅ CCH	$\sim 2.5 \times 10^{12}$	2.5×10^{-10}	2,C
C ₆ H ₅ CN	1.2×10^{12}	1.2×10^{-10}	2,D
<i>c</i> -C ₉ H ₈	1.6×10^{13}	1.6×10^{-09}	1,E

Notes.

^(a) Assuming a column density of molecular hydrogen of 10^{22} cm^{-2} (Cernicharo & Guélin, 1987). We note that there is a significant difference in the beam size for the QUIJOTE and GOTHAM line surveys. This could explain, at least partially, the differences in the derived parameters. ⁽¹⁾ Cernicharo et al. (2021a). ⁽²⁾ This work. ^(A) A value of $1.44 \times 10^{12} \text{ cm}^{-2}$ was reported by McCarthy et al. (2021) and of $8.3 \times 10^{11} \text{ cm}^{-2}$ by Lee et al. (2021). ^(B) A value of $1.9 \times 10^{11} \text{ cm}^{-2}$ was derived by Lee et al. (2021). ^(C) Tentative detection. ^(D) A value of $4.0 \times 10^{11} \text{ cm}^{-2}$ was derived by McGuire et al. (2018). This value was revised to $1.6 \times 10^{11} \text{ cm}^{-2}$ by Burkhardt et al. (2021). ^(E) A value of $9.6 \times 10^{12} \text{ cm}^{-2}$ was reported by Burkhardt et al. (2021).

(2021d). We also included a specific chemistry for the CCH and CN derivatives of *c*-C₅H₆ and C₆H₆. We assumed that they are destroyed through reactions with C, C⁺, and H⁺. The chemical scheme of formation of these species is based on neutral-neutral reactions and is discussed in detail in Appendix D. Briefly, reactions of CCH and CN with *c*-C₅H₆ and C₆H₆ lead to the CCH/CN derivatives of each cycle (Balucani et al., 1999; Jones et al., 2010). The formation of the precursor hydrocarbon cycles *c*-C₅H₆ and C₆H₆ relies on reactions between small hydrocarbon radicals and butadiene (CH₂CHCHCH₂), which acts as a key species that opens the chemistry to hydrocarbon cycles at 10 K (He et al., 2020a; Jones et al., 2011). Additional routes to the CCH/CN derivatives of *c*-C₅H₆ involve reactions of C₃H/C₂N with butadiene. The chemical scheme thus involves essentially neutral-neutral reactions, with the exception of benzene, which has been hypothesized to also be formed by a route involving ion-neutral reactions that result in the precursor ion C₆H₇⁺ (see e.g. Agúndez et al. 2021a).

If we set the gas-phase elemental abundance of oxygen to $O/H = 3.3 \times 10^{-4}$ ($C/O = 0.55$), the calculated peak abundances of all CCH/CN derivatives of *c*-C₅H₆ and C₆H₆ remain two to three orders of magnitude below the observed values. If the gas-phase elemental abundance of oxygen is decreased so that $C/O = 1$ ($O/H = 1.8 \times 10^{-4}$), then the agreement between the chemical model and the observations is much better (see Fig. 3). Producing *c*-C₅H₆ with an abundance as high as $\sim 10^{-9}$ relative to H₂ and CCH/CN derivatives of *c*-C₅H₆ and C₆H₆ with abundances in the range 10^{-11} - 10^{-10} seems to require a C/O elemental gas-phase ratio close to that in TMC-1. This is in agreement with a recent study on the elemental abundances in TMC-1 (Fuente et al., 2019).

A significant failure of the chemical model concerns the abundance ratios between the CCH and the CN derivatives of both *c*-C₅H₆ and C₆H₆, which are below one, while the observed ones are above unity. This is ultimately caused by the overabundance of CN in the chemical model, a feature also found in previous chemical models of cold dark clouds (e.g. Agúndez & Wakelam 2013; Daranlot et al. 2013), which deserves a dedicated study. As a consequence, the calculated CCH/CN ratio is < 1 at any time (see the left panel in Fig. 3), while the observed

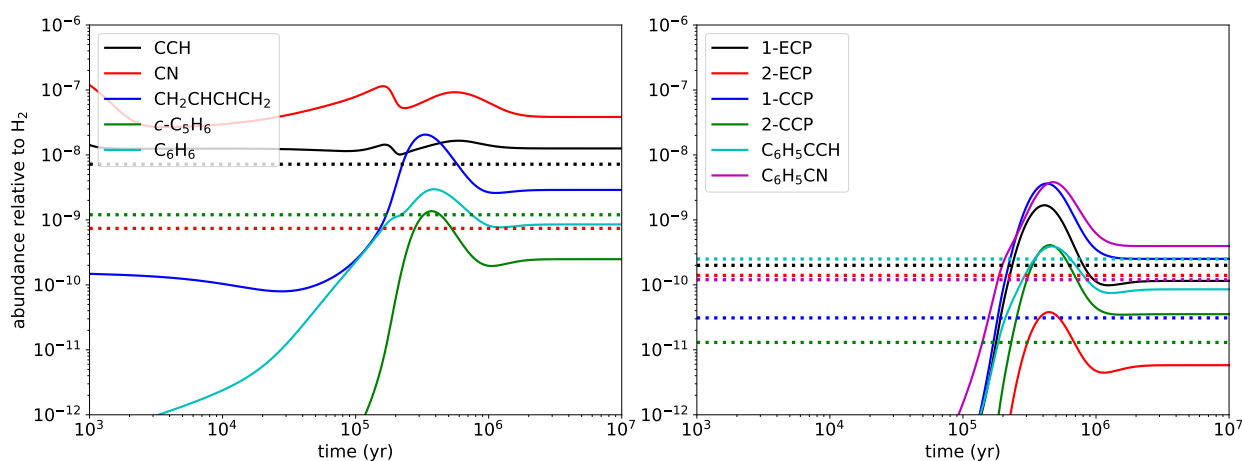


Fig. 3. Calculated abundances of CCH and CN derivatives of $c\text{-C}_5\text{H}_6$ and C_6H_6 (right panel) and of their precursors (left panel). The horizontal dotted lines correspond to the abundances observed in TMC-1.

CCH/CN ratio in TMC-1 is ~ 10 (Pratap et al., 1997). This fact translates to the CCH and CN derivatives of $c\text{-C}_5\text{H}_6$ and C_6H_6 , for which calculated CCH/CN ratios are < 1 , while the observed ones are > 1 (see the right panel in Fig. 3). It is worth noting that the CCH/CN ratio observed for cyclopentadiene, $(1\text{-ECP} + 2\text{-ECP})/(1\text{-CCP} + 2\text{-CCP}) = 7.7$, is close to the CCH/CN ratio itself, ~ 10 (Pratap et al., 1997), while the CCH/CN ratio for benzene, $\text{C}_6\text{H}_5\text{CCH}/\text{C}_6\text{H}_5\text{CN} \leq 2.1$, is significantly lower. This fact suggests that additional routes to the reaction $\text{CN} + \text{C}_6\text{H}_6$ could form $\text{C}_6\text{H}_5\text{CN}$ in TMC-1. In the case of the CCH and CN derivatives of C_3H_4 , the CCH/CN ratio is 3.5 (Marcelino et al., 2021; Cernicharo et al., 2021b), which is in between the values found for the derivatives of $c\text{-C}_5\text{H}_6$ and C_6H_6 .

Concerning the abundance ratios between different isomers, for $c\text{-C}_5\text{H}_5\text{CCH}$ the two isomers 1-ECP and 2-ECP are observed with similar abundances. However, the chemical model calculates 1-ECP to be much more abundant than 2-ECP (see the right panel in Fig. 3) because, in addition to the reaction $\text{C}_2\text{H} + c\text{-C}_5\text{H}_6$, which produces the two isomers, the reaction between C_3H and butadiene yields 1-ECP but not 2-ECP (see Appendix D). Similarly, for $c\text{-C}_5\text{H}_5\text{CN}$ the chemical model calculates a 1-CCP/2-CCP ratio higher than observed because 1-CCP has more formation routes. We note, however, that the branching ratios adopted in the chemical model for the production of the different isomers are uncertain.

A success of the chemical model is that it correctly reproduces the abundance of cyclopentadiene. If the chemical scheme discussed in Appendix D is complete, the abundances of the non-polar molecules benzene and butadiene in TMC-1 should be of the order of the calculated ones. That is, benzene should be present with an abundance of some 10^{-9} relative to H_2 , similar to that of cyclopentadiene, while butadiene should be around ten times more abundant than benzene (see the left panel in Fig. 3). If butadiene is that abundant, it could be detected indirectly, for example through its protonated form or a polar derivative such as $\text{C}_4\text{H}_5\text{CN}$.

5. Conclusions

We have reported the detection in TMC-1 of two isomers of ethynyl cyclopentadiene ($c\text{-C}_5\text{H}_5\text{CCH}$), namely 1-ECP and 2-ECP, and the tentative detection of EBZ ($\text{C}_6\text{H}_5\text{CCH}$). In addition, we report an exhaustive line-by-line detection of the cyano derivatives of cyclopentadiene and benzene ($c\text{-C}_5\text{H}_5\text{CN}$

and $\text{C}_6\text{H}_5\text{CN}$). This allowed us to provide a coherent set of column densities for the various CCH and CN derivatives of cyclopentadiene and benzene in TMC-1. A chemical model that includes chemical routes to these cycles based on neutral-neutral reactions is reasonably successful in explaining the order of magnitude of the observed abundances. It is predicted that benzene should have an abundance similar to that of cyclopentadiene in TMC-1.

Acknowledgements. We thank ERC for funding through grant ERC-2013-SyG-610256-NANOCOSMOS and Ministerio de Ciencia e Innovación of Spain (MICIU) for funding support through projects PID2019-106110GB-I00, PID2019-107115GB-C21, and PID2019-106235GB-I00. M.A. thanks MICIU for grant RyC-2014-16277.

References

- Agúndez, M. & Wakelam, V. 2013, *Chem. Rev.* 113, 8710
 Agúndez, M., Cabezas, C., Tercero, B., et al. 2021a, *A&A*, 647, L10
 Agúndez, M., Marcelino, N., Tercero, B., et al. 2021b, *A&A*, 649, L4
 Balucani, N., Asvany, O., Chang, A.H.H. et al. 1999, *J. Chem. Phys.*, 111, 7457
 Bodi, J., Oomens, J. & Hemberger, P. 2015, *PCCP*, 17, 20508
 Burkhardt, A.M., Loomis, R.A., Shingledecker, C.N., et al. 2021, *Nature Astron.*, 5, 181
 Cernicharo, J. 1985, Internal IRAM report (Granada: IRAM)
 Cernicharo, J. & Guélin, M. 1987, *A&A*, 176, 299
 Cernicharo, J., 2012, in *ECLA 2011: Proc. of the European Conference on Laboratory Astrophysics*, EAS Publications Series, 2012, Ed.: C. Stehl, C. Joblin, & L. d'Hendecourt (Cambridge: Cambridge Univ. Press), 251; https://nanocosmos.iff.csic.es/?page_id=1619
 Cernicharo, J., Marcelino, N., Agúndez, M. et al. 2020, *A&A*, 642, L8
 Cernicharo, J., Agúndez, M., Cabezas, C., et al. 2021a, *A&A*, 649, L15
 Cernicharo, J., Agúndez, M., Cabezas, C., et al. 2021b, *A&A*, 647, L2
 Cernicharo, J., Cabezas, C., Agúndez, M., et al. 2021c, *A&A*, 647, L3
 Cernicharo, J., Agúndez, M., Kaiser, R., et al. 2021d, *A&A*, 652, L9
 Cernicharo, J., Cabezas, C., Endo, Y., et al. 2021e, *A&A*, 646, L3
 Cooke, I. R., Gupta, D., Massinger, J. P., & Sims, I. R. 2020, *ApJ*, 891, L41
 Cox, A.P., Ewart, I.C. & Stigliani, W.M. 1975, *J. Chem. Soc. Faraday Trans. II*, 71, 504
 Daranlot, J., Hu, X., Xie, C., et al. 2013, *PCCP*, 15, 13888
 da Silva, G., Cole, J.A. & Bozzelli, J.W. 2010, *J. Phys. Chem. A*, 114, 2275
 da Silva, G. 2017, *J. Phys. Chem. A*, 121, 2086
 Dreizler, H., Rudolph, H.D. & Hartke, B. 2004, *J. Mol. Struct.*, 698, 1
 Ford, R.G. & Seitzman, H.A. 1978, *J. Mol. Spectrosc.*, 69, 326
 Fossé, D., Cernicharo, J., Gerin, M., Cox, P. 2001, *ApJ*, 552, 168
 Frisch, M. J., Pople J. A. & Binkley, J. S., 1984, *J. Chem. Phys.*, 80, 3265.
 Fuente, A., Navarro, D. G., Caselli, P., et al. 2019, *A&A*, 624, A105
 Goulay, F. & Leone, S. R. 2006, *J. Phys. Chem. A*, 110, 1875
 He, C., Zhao, L., Doddipatla, S., et al. 2020a, *Chem. Phys. Chem.*, 21, 1295
 He, C., Thomas, M., Galimova, G.R., et al. 2020b, *JACS*, 142, 3205
 Jones, B.M., Zhang, F., Maksyutenko, P. et al. 2010, *J. Phys. Chem. A*, 114, 5256

- Jones, B.M., Zhang, F., Kaiser, R.I., 2011, PNAS, 108, 452
- Kaiser, R. & Hansen, N. 2021, J. Chem. Phys. A, 125, 3826
- Kaiser, R., Goswami, M., Maksyutenko, P. et al. 2011, J. Phys. Chem. A, 115, 10258
- Kisiel, Z. & Kraśnicki, A. 2010, J. Mol. Spectrosc., 262, 82
- Lee, K.L.K. & McCarthy, M.C. 2019, J. Phys. Chem. Lett., 10, 2408
- Lee, K.L.K., Changala, P.B., Loomis, R.A., et al. 2021, ApJ, 910, L2
- Loison, J.-C., Hébrard, E., Dobrijevic, M., et al. 2015, Icarus, 247, 218
- Marcelino, N., Tercero, B., Agúndez, M., & Cernicharo, J., 2021, A&A, 646, L9
- McCarthy, M.C., Lee, K.L.K., Carroll, P.B. et al. 2020, J. Phys. Chem. A, 124, 5170
- McCarthy, M.C., Lee, K.L.K., Loomis, R.A., et al. 2021, Nature Astron., 5, 176
- McElroy, D., Walsh, C., Markwick, A. J., et al. 2013, A&A, 550, A36
- McGuire, B.A., Burkhardt, A.M., Kalenskii, S., et al. 2018, Science, 359, 202
- McGuire, B.A., Loomis, R.A., Burkhardt, A.M., et al. 2021, Science, 371, 1265
- Møller, C., & Plesset, M. S., 1934, Phys. Rev. 46, 618
- Müller, H.S.P., Schlöder, F., Stutzki, J., Winnewisser, G. 2005, J. Mol. Struct., 742, 215
- Pardo, J. R., Cernicharo, J., Serabyn, E. 2001, IEEE Trans. Antennas and Propagation, 49, 12
- Pickett, H.M., Poynter, R. L., Cohen, E. A., et al. 1998, J. Quant. Spectrosc. Radiat. Transfer, 60, 883
- Pratap, P., Dickens, J. E., Snell, R. L., et al. 1997, ApJ, 486, 862
- Sakaizumi, T., Kikuchi, H., Ohashi, O. & Yamaguchi, I. 1987, Bull. Chem. Soc. Jpn., 60, 3903
- Tercero, F., López-Pérez, J. A., Gallego, J.D. et al. 2021, A&A, 645, A37
- Zhang, F., Parker, D.S.N., Kim, Y.S., et al. 2011, ApJ, 728, 141

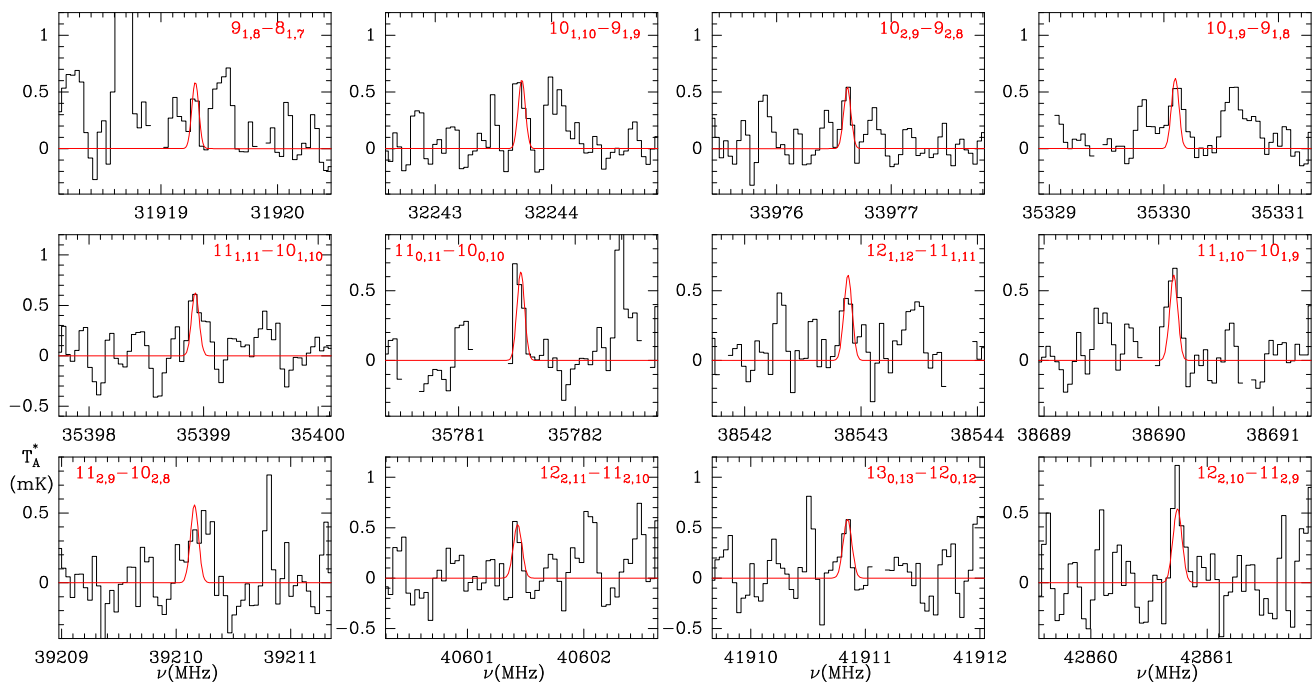


Fig. A.1. Observed lines of 1-*ECP* in the 31-50 GHz frequency range towards TMC-1. Line parameters for the complete list of detected lines of 1-*ECP* are given in Table A.2. The abscissa corresponds to the rest frequency assuming a local standard of rest velocity of 5.83 km s⁻¹. The ordinate is the antenna temperature corrected for atmospheric and telescope losses in mK. The red line shows the synthetic spectrum obtained for an assumed T_r of 9 K and $N(1\text{-}ECP)=(2.0\pm 0.4)\times 10^{12}$ cm⁻². The rotational quantum numbers are indicated in each panel. Blanked channels correspond to negative features produced in the folding of the frequency switching data.

Appendix A: Observed lines of 1-*ECP*, 2-*ECP*, and *EBZ*

Line parameters were derived from a Gaussian fit to the observed lines using the GILDAS package. A velocity coverage of ± 15 km s⁻¹ was selected for each line. Observed frequencies were derived assuming a local standard of rest velocity of 5.83 km s⁻¹ (Cernicharo et al., 2020). The predicted frequencies in MADEX (Cernicharo, 2012), which arise from a fit to the laboratory data of McCarthy et al. (2020), agree within 5-30 kHz with the observed ones. These differences are always below $2\times\sigma\times\Delta\nu$, where $\Delta\nu$ is the estimated frequency uncertainty of the observed lines. The derived line parameters for 2-*ECP* and 1-*ECP* are given in Tables A.1 and A.2, respectively. Selected lines of 1-*ECP* and 2-*ECP* are shown in Figs. A.1 and 2, respectively. A merged fit to the laboratory and TMC-1 frequencies is discussed in Appendix A.1.

Table A.1. Observed line parameters of 2-ECP.

Transition ($J_{K_a,K_c})_u - (J_{K_a,K_c})_l$	ν_{pred}^a (MHz)	ν_{obs}^b (MHz)	$\int T_A^* dv^c$ (mK km s ⁻¹)	$\Delta\nu^d$ (km s ⁻¹)	T_A^{*e} (mK)	N
9 _{2,7} – 8 _{2,6}	31804.974±0.010	31804.956±0.010	0.81±0.14	0.88±0.16	0.87±0.18	
9 _{1,8} – 8 _{1,7}	31836.466±0.009	31836.469±0.010	0.80±0.21	1.01±0.25	0.74±0.18	
10 _{1,10} – 9 _{1,9}	32128.912±0.006	32128.929±0.020	0.50±0.12	0.82±0.23	0.57±0.16	
10 _{0,10} – 9 _{0,9}	32584.193±0.006					A
10 _{2,9} – 9 _{2,8}	33877.354±0.008				≤0.54	B
10 _{3,8} – 9 _{3,7}	34371.631±0.010	34371.645±0.020	0.35±0.13	0.53±0.22	0.63±0.16	
10 _{3,7} – 9 _{3,6}	34598.278±0.012	34598.267±0.010	0.47±0.10	0.68±0.20	0.65±0.16	
10 _{1,9} – 9 _{1,8}	35232.520±0.012	35232.541±0.010	0.44±0.08	0.70±0.15	0.59±0.16	
11 _{1,11} – 10 _{1,10}	35271.182±0.009	35271.206±0.020	0.25±0.06	0.33±0.20	0.65±0.17	C
10 _{2,8} – 9 _{2,7}	35477.328±0.015				≤0.55	
11 _{0,11} – 10 _{0,10}	35640.891±0.008	35640.883±0.010	0.30±0.09	0.58±0.17	0.50±0.17	
11 _{2,10} – 10 _{2,9}	37187.287±0.010	37187.341±0.020	0.40±0.12	1.12±0.30	0.34±0.16	
11 _{3,9} – 10 _{3,8}	37818.228±0.014				≤0.52	
11 _{3,8} – 10 _{3,7}	38176.533±0.017	38176.490±0.010	0.77±0.14	1.02±0.21	0.70±0.16	D
12 _{1,12} – 11 _{1,11}	38402.186±0.012	38402.176±0.010	0.40±0.09	0.61±0.16	0.62±0.16	
11 _{1,10} – 10 _{1,9}	38575.843±0.015	38575.866±0.010	0.53±0.12	0.54±0.13	0.54±0.16	
12 _{0,12} – 11 _{0,11}	38692.902±0.012	38692.899±0.010	0.41±0.08	0.57±0.15	0.67±0.17	
11 _{2,9} – 10 _{2,8}	39139.995±0.021	39140.044±0.030	0.46±0.14	0.97±0.30	0.45±0.17	
12 _{2,11} – 11 _{2,10}	40476.885±0.014					E
12 _{3,10} – 11 _{3,9}	41258.658±0.019	41258.707±0.020	0.45±0.18	0.50±0.18	0.90±0.26	E
13 _{1,13} – 12 _{1,12}	41523.491±0.016	41523.514±0.020	0.42±0.15	0.62±0.25	0.63±0.24	
13 _{0,13} – 12 _{0,12}	41746.171±0.016	41746.185±0.020	0.53±0.17	0.89±0.27	0.56±0.25	
12 _{3,9} – 11 _{3,8}	41795.647±0.024	41795.617±0.020	0.30±0.11	0.54±0.20	0.53±0.20	
12 _{1,11} – 11 _{1,10}	41860.507±0.018	41860.552±0.010	0.39±0.09	0.40±0.15	0.99±0.20	
12 _{2,10} – 11 _{2,9}	42779.782±0.028	42779.776±0.020	0.37±0.10	0.66±0.25	0.52±0.20	F
13 _{2,12} – 12 _{2,11}	43745.506±0.017				≤0.62	
14 _{1,14} – 13 _{1,13}	44636.685±0.021	44636.635±0.010	0.51±0.13	0.55±0.15	0.88±0.24	
14 _{0,14} – 13 _{0,13}	44803.670±0.021	44803.652±0.010	1.05±0.15	0.59±0.10	1.68±0.26	D
13 _{1,12} – 12 _{1,11}	45083.511±0.021	45083.564±0.020	0.62±0.15	0.48±0.13	1.21±0.30	
13 _{3,10} – 12 _{3,9}	45456.801±0.033	45456.835±0.020	0.38±0.10	0.25±0.20	1.43±0.30	
13 _{2,11} – 12 _{2,10}	46386.401±0.036				≤0.9	
14 _{2,13} – 13 _{2,12}	46992.950±0.021	46992.978±0.010	0.60±0.16	0.44±0.14	1.26±0.30	
15 _{1,15} – 14 _{1,14}	47743.272±0.027				≤0.9	
15 _{0,15} – 14 _{0,14}	47866.359±0.027				≤1.0	

Notes.

- For the observational parameters we adopted the uncertainty of the Gaussian fit provided by GILDAS. Upper limits correspond to 3σ values.
- (*a*) Predicted frequency from the rotational and distortion constants derived from a fit to the lines observed by McCarthy et al. (2020) (see Sect. 3.1.1).
- (*b*) Observed frequency assuming a v_{LSR} of 5.83 km s⁻¹.
- (*c*) Integrated line intensity in mK km s⁻¹.
- (*d*) Line width at half intensity derived by fitting a Gaussian function to the observed line profile (in km s⁻¹).
- (*e*) Antenna temperature in millikelvin.
- (*A*) Blended with a negative feature resulting from the folding of the frequency switching data.
- (*B*) Possible blend with a negative feature (see note A). Fit unreliable.
- (*C*) Partially blended with a negative feature (see note A). Fit still possible.
- (*D*) Possible blend with an unidentified line. The line appears too strong compared with other transitions.
- (*E*) Fully blended with one of the hyperfine components of H₂CCN.
- (*F*) Possible blend with an unidentified line. The derived intensity is in line with that of other transitions.

Table A.2. Observed line parameters of 1-*ECP*.

Transition ($J_{K_a,K_c})_u - (J_{K_a,K_c})_l$	ν_{pred}^a (MHz)	ν_{obs}^b (MHz)	$\int T_A^* dv^c$ (mK km s ⁻¹)	Δv^d (km s ⁻¹)	T_A^{*e} (mK)	N
9 _{3,6} – 8 _{3,5}	31125.481±0.003				≤0.53	
9 _{2,7} – 8 _{2,6}	31859.742±0.004				≤0.55	
9 _{1,8} – 8 _{1,7}	31919.294±0.003	31919.294±0.020	0.35±0.09	0.55±0.25	0.44±0.15	A
10 _{1,10} – 9 _{1,9}	32243.744±0.006	32243.721±0.015	0.61±0.11	0.91±0.18	0.64±0.14	
10 _{0,10} – 9 _{0,9}	32711.504±0.005					B
10 _{2,9} – 9 _{2,8}	33976.618±0.005	33976.611±0.010	0.44±0.10	0.73±0.18	0.57±0.15	
10 _{3,8} – 9 _{3,7}	34456.710±0.004				≤0.55	
10 _{3,7} – 9 _{3,6}	34670.863±0.005				≤0.51	
10 _{1,9} – 9 _{1,8}	35330.100±0.004	35330.107±0.010	0.80±0.14	1.20±0.30	0.52±0.16	
11 _{1,11} – 10 _{1,10}	35398.929±0.008	35398.938±0.020	0.57±0.15	0.82±0.29	0.65±0.18	
10 _{2,8} – 9 _{2,7}	35538.796±0.005				≤0.50	C
11 _{0,11} – 10 _{0,10}	35781.534±0.008	35781.525±0.010	0.54±0.10	0.73±0.15	0.70±0.18	
11 _{2,10} – 10 _{2,9}	37298.932±0.006				≤0.50	D
11 _{3,9} – 10 _{3,8}	37912.444±0.005				≤0.55	
11 _{3,8} – 10 _{3,7}	38251.486±0.007				≤0.59	
12 _{1,12} – 11 _{1,11}	38542.888±0.011	38542.877±0.015	0.28±0.08	0.71±0.22	0.37±0.13	
11 _{1,10} – 10 _{1,9}	38690.146±0.005	38690.125±0.015	0.71±0.12	0.98±0.18	0.65±0.14	
12 _{0,12} – 11 _{0,11}	38845.920±0.011				≤0.51	
11 _{2,9} – 10 _{2,8}	39210.161±0.007	39210.148±0.020	0.35±0.10	0.77±0.30	0.41±0.16	E
12 _{2,11} – 11 _{2,10}	40601.469±0.009	40601.428±0.020	0.27±0.09	0.28±0.15	0.55±0.20	F
12 _{3,10} – 11 _{3,9}	41362.551±0.007				≤<0.60	
13 _{1,13} – 12 _{1,12}	41677.124±0.015				≤<0.66	G
12 _{3,9} – 11 _{3,8}	41871.672±0.009				≤<0.70	
13 _{0,13} – 12 _{0,12}	41910.880±0.015	41910.870±0.015	0.37±0.12	0.60±0.25	0.58±0.18	
12 _{1,11} – 11 _{1,10}	41993.447±0.007	41993.453±0.025	0.64±0.15	0.70±0.32	0.86±0.20	H
12 _{2,10} – 11 _{2,9}	42860.722±0.010	42860.741±0.015	0.54±0.14	0.61±0.19	0.83±0.22	
13 _{2,12} – 12 _{2,11}	43883.551±0.011				≤0.60	
14 _{1,14} – 13 _{1,13}	44803.174±0.019				≤0.76	
13 _{3,11} – 12 _{3,10}	44804.061±0.009				≤0.69	
14 _{0,14} – 13 _{0,13}	44979.670±0.019				≤0.87	
13 _{1,12} – 12 _{1,11}	45236.599±0.010				≤0.92	
13 _{3,10} – 12 _{3,9}	45533.079±0.013				≤1.05	
13 _{2,11} – 12 _{2,10}	46480.158±0.012				≤0.91	
14 _{2,13} – 13 _{2,12}	47144.916±0.015				≤1.15	
15 _{1,15} – 14 _{1,14}	47922.512±0.025					I
15 _{0,15} – 14 _{0,14}	48053.480±0.025				≤1.15	
14 _{3,12} – 13 _{3,11}	48234.023±0.012				≤1.25	
14 _{1,13} – 13 _{1,12}	48420.229±0.013	48420.188±0.015	0.55±0.13	0.48±0.12	1.0±0.29	
14 _{3,11} – 13 _{3,10}	49233.211±0.017				≤1.18	

Notes.

For the observational parameters we adopted the uncertainty of the Gaussian fit provided by GILDAS. Upper limits correspond to 3 σ values.

(^a) Predicted frequency from the rotational and distortion constants derived from a fit to the lines observed by McCarthy et al. (2020) (see Sect. 3.1.2).

(^b) Observed frequency assuming a v_{LSR} of 5.83 km s⁻¹.

(^c) Integrated line intensity in mK km s⁻¹.

(^d) Line width at half intensity derived by fitting a Gaussian function to the observed line profile (in km s⁻¹).

(^e) Antenna temperature in millikelvin.

(A) Marginal detection.

(B) Blended with the $J=29-28$ transition of HC₇N at 32711.672 MHz.

(C) A 2.5 σ feature appears at the predicted frequency.

(D) A 0.4 mK feature appears at -83 kHz of the predicted frequency. The line profile is affected in its blue frequency wing by a negative feature produced in the folding of the frequency switching data. Fit unreliable.

(E) The line is blended with two unidentified features. Doubtful fit.

(F) Possible blend with a negative feature in the red wing of the line profile. Doubtful fit.

(G) Feature of 0.5 mK at -130 kHz. It cannot be assigned to 1-*ECP*.

(H) The line is blended in its red wing with a unknown feature. Doubtful fit.

(I) The line is fully blended with a negative feature produced in the folding of the frequency switching data.

Table A.3. Rotational and distortion constants for 1-*ECP* and 2-*ECP*.

Constant	1- <i>ECP</i> ^a (MHz)	1- <i>ECP</i> ^b (MHz)	2- <i>ECP</i> ^c (MHz)	2- <i>ECP</i> ^b (MHz)
<i>A</i>	8374.116845(672)	8374.116982(777)	8262.3702(10)	8262.3708(15)
<i>B</i>	1879.207441(354)	1879.206888(286)	1876.250982(284)	1876.252295(342)
<i>C</i>	1549.116825(323)	1549.117494(236)	1543.195532(187)	1543.194285(305)
$\Delta_J 10^{-5}$	6.862(218)	6.643(162)	4.879(292)	5.646(179)
$\Delta_{JK} 10^{-3}$	2.4044(163)	2.4271(154)	2.5504(205)	2.5219(288)
$\delta_J 10^{-5}$	1.815(113)	1.6858(645)	1.082(216)	1.0217(707)
$\delta_K 10^{-4}$	15.59(145)	13.04(106)		6.98(113)
N_{lines}	30	44	39	63
ν_{max} (GHz)	24.974	48.420	25.805	46.992
$(J, K_a)_{max}$	7,3	14,3	8,3	14,3
σ (kHz)	1.3	8.3	3.0	16.0

Notes.

Values between parentheses correspond to the uncertainties of the parameters in units of the last significant digits.

^(a) Rotational and distortion constants from a fit to the lines of 1-*ECP* measured in the laboratory by McCarthy et al. (2020), including the distortion constant δ_K .

^(b) Merged fit to the laboratory and space frequencies.

^(c) Rotational and distortion constants from a fit to lines of 2-*ECP* measured in the laboratory by McCarthy et al. (2020) with the uncertainties of 2 kHz changed to 4 kHz.

Appendix A.1: Improved rotational constants for 1-*ECP* and 2-*ECP*

The observed lines of 2-*ECP* (see Table A.1) and 1-*ECP* (see Table A.2) were merged with the laboratory data (McCarthy et al., 2020) to provide a new set of rotational and distortion constants. They are given in Table A.3 and can be used to predict the frequencies of the rotational transitions for the two observed isomers of cyclopentadiene up to 50 GHz with an accuracy better than 15 kHz ($K_a \leq 3$). The calculated and the observed-minus-calculated frequencies for 2-*ECP* and 1-*ECP* are given in Tables A.4 and A.5, respectively.

Table A.4. Observed and calculated line frequencies for 2-*ECP*.

Transition	ν_{obs}^a (MHz)	ν_{cal}^b (MHz)	$\nu_{obs}-\nu_{cal}^c$ (MHz)	Notes
2 _{1,2} – 1 _{1,1}	6505.8227±0.004	6505.8264±0.0005	-0.0037	1
1 _{1,0} – 1 _{0,1}	6719.1716±0.004	6719.1700±0.0014	0.0016	1
2 _{0,2} – 1 _{0,1}	6826.2008±0.004	6826.2014±0.0005	-0.0006	1
2 _{1,1} – 2 _{0,2}	7064.9046±0.004	7064.9047±0.0015	-0.0001	1
2 _{1,1} – 1 _{1,0}	7171.9370±0.004	7171.9361±0.0006	0.0010	1
3 _{1,2} – 3 _{0,3}	7607.0222±0.004	7607.0213±0.0016	0.0009	1
4 _{0,4} – 3 _{1,3}	7942.9745±0.004	7942.9736±0.0018	0.0010	1
4 _{1,3} – 4 _{0,4}	8372.6059±0.004	8372.6036±0.0021	0.0023	1
5 _{1,4} – 5 _{0,5}	9394.8545±0.004	9394.8561±0.0028	-0.0016	1
1 _{1,1} – 0 _{0,0}	9805.5638±0.004	9805.5612±0.0015	0.0026	1
3 _{1,3} – 2 _{1,2}	9750.9497±0.004	9750.9517±0.0007	-0.0020	1
3 _{0,3} – 2 _{0,2}	10207.6962±0.004	10207.6961±0.0007	0.0002	1
3 _{2,2} – 2 _{2,1}	10258.2745±0.004	10258.2731±0.0007	0.0014	1
3 _{2,1} – 2 _{2,0}	10308.9078±0.004	10308.9107±0.0007	-0.0029	1
3 _{1,2} – 2 _{1,1}	10749.8126±0.004	10749.8126±0.0008	-0.0000	1
5 _{0,5} – 4 _{1,4}	11804.6273±0.004	11804.6243±0.0020	0.0030	1
2 _{1,2} – 1 _{0,1}	12891.9402±0.004	12891.9412±0.0016	-0.0010	1
4 _{1,4} – 3 _{1,3}	12987.1482±0.004	12987.1487±0.0009	-0.0005	1
4 _{0,4} – 3 _{0,3}	13551.9681±0.004	13551.9690±0.0009	-0.0009	1
4 _{2,3} – 3 _{2,2}	13667.8217±0.004	13667.8189±0.0009	0.0028	1
4 _{3,2} – 3 _{3,1}	13702.0907±0.004	13702.0855±0.0017	0.0052	1
4 _{3,1} – 3 _{3,0}	13703.8882±0.004	13703.8985±0.0017	-0.0103	1
4 _{2,2} – 3 _{2,1}	13793.6166±0.004	13793.6158±0.0009	0.0008	1
4 _{1,3} – 3 _{1,2}	14317.5513±0.004	14317.5513±0.0010	-0.0000	1
6 _{0,6} – 5 _{1,5}	15684.0022±0.004	15684.0029±0.0022	-0.0007	1
5 _{1,5} – 4 _{1,4}	16212.1187±0.004	16212.1190±0.0011	-0.0003	1
5 _{0,5} – 4 _{0,4}	16848.7979±0.004	16848.7994±0.0011	-0.0015	1
5 _{2,4} – 4 _{2,3}	17068.9149±0.004	17068.9111±0.0011	0.0038	1
5 _{3,3} – 4 _{3,2}	17137.5081±0.004	17137.5036±0.0020	0.0045	1
5 _{3,2} – 4 _{3,1}	17143.8417±0.004	17143.8366±0.0020	0.0051	1
5 _{2,3} – 4 _{2,2}	17317.2679±0.004	17317.2686±0.0011	-0.0007	1
5 _{1,4} – 4 _{1,3}	17871.0508±0.004	17871.0519±0.0012	-0.0011	1
4 _{1,4} – 3 _{0,3}	18596.1415±0.004	18596.1441±0.0022	-0.0026	1
6 _{1,6} – 5 _{1,5}	19424.1049±0.004	19424.1046±0.0012	0.0003	1
6 _{0,6} – 5 _{0,5}	20091.4959±0.004	20091.4977±0.0013	-0.0018	1
6 _{1,5} – 5 _{1,4}	21405.5877±0.004	21405.5901±0.0013	-0.0024	1
7 _{1,7} – 6 _{1,6}	22621.9636±0.004	22621.9644±0.0014	-0.0008	1
7 _{1,6} – 6 _{1,5}	24915.6787±0.010	24915.6815±0.0016	-0.0028	1
8 _{1,8} – 7 _{1,7}	25805.2041±0.004	25805.2049±0.0015	-0.0008	1
9 _{2,7} – 8 _{2,6}	31804.9560±0.010	31804.9681±0.0036	-0.0121	2
9 _{1,8} – 8 _{1,7}	31836.4690±0.010	31836.4750±0.0024	-0.0060	2
10 _{1,10} – 9 _{1,9}	32128.9290±0.020	32128.9081±0.0021	0.0209	2
10 _{3,8} – 9 _{3,7}	34371.6450±0.020	34371.6387±0.0036	0.0064	2
10 _{3,7} – 9 _{3,6}	34598.2670±0.010	34598.2718±0.0042	-0.0048	2
10 _{1,9} – 9 _{1,8}	35232.5410±0.010	35232.5337±0.0031	0.0073	2
11 _{1,11} – 10 _{1,10}	35271.2060±0.020	35271.1752±0.0026	0.0308	2
11 _{0,11} – 10 _{0,10}	35640.8830±0.010	35640.8855±0.0026	-0.0025	2
11 _{2,10} – 10 _{2,9}	37187.3410±0.020	37187.3126±0.0043	0.0284	2
11 _{3,8} – 10 _{3,7}	38176.4900±0.010	38176.5234±0.0057	-0.0334	2
12 _{1,12} – 11 _{1,11}	38402.1760±0.010	38402.1750±0.0035	0.0010	2
11 _{1,10} – 10 _{1,9}	38575.8660±0.010	38575.8633±0.0038	0.0027	2
12 _{0,12} – 11 _{0,11}	38692.9020±0.010	38692.8915±0.0035	0.0105	2
11 _{2,9} – 10 _{2,8}	39140.0440±0.030	39139.9920±0.0067	0.0520	2
12 _{3,10} – 11 _{3,9}	41258.7070±0.020	41258.6781±0.0052	0.0289	2
13 _{1,13} – 12 _{1,12}	41523.5140±0.020	41523.4740±0.0047	0.0400	2
13 _{0,13} – 12 _{0,12}	41746.1850±0.020	41746.1544±0.0047	0.0306	2
12 _{3,9} – 11 _{3,8}	41795.6170±0.020	41795.6321±0.0075	-0.0151	2
12 _{1,11} – 11 _{1,10}	41860.5520±0.010	41860.5363±0.0049	0.0157	2
12 _{2,10} – 11 _{2,9}	42779.7760±0.020	42779.7823±0.0085	-0.0063	2
14 _{1,14} – 13 _{1,13}	44636.6350±0.010	44636.6596±0.0063	-0.0246	2
14 _{0,14} – 13 _{0,13}	44803.6520±0.010	44803.6444±0.0063	0.0076	2
13 _{1,12} – 12 _{1,11}	45083.5640±0.020	45083.5500±0.0062	0.0140	2
13 _{3,10} – 12 _{3,9}	45456.8350±0.020	45456.7837±0.0112	0.0513	2
14 _{2,13} – 13 _{2,12}	46992.9780±0.010	46992.9999±0.0088	-0.0219	2

Notes.^(a) Observed line frequencies and assigned uncertainties.^(b) Calculated frequencies and uncertainties.^(c) Observed-minus-calculated frequencies.⁽¹⁾ Laboratory data from McCarthy et al. (2020).⁽²⁾ Frequencies observed in TMC-1 assuming a v_{LSR} of 5.83 km s⁻¹ (see Table A.1).

Table A.5. Observed and calculated line frequencies for 1-*ECP*.

Transition	ν_{obs}^a (MHz)	ν_{cal}^b (MHz)	$\nu_{obs}-\nu_{cal}^c$ (MHz)	Notes
2 _{1,2} – 1 _{1,1}	6526.5517±0.002	6526.5533±0.0002	-0.0016	1
1 _{1,0} – 1 _{0,1}	6824.9928±0.002	6824.9920±0.0008	0.0008	1
2 _{0,2} – 1 _{0,1}	6844.3837±0.002	6844.3828±0.0002	0.0009	1
2 _{1,1} – 1 _{1,0}	7186.7197±0.002	7186.7206±0.0003	-0.0009	1
5 _{1,4} – 5 _{0,5}	9468.7286±0.002	9468.7268±0.0012	0.0018	1
3 _{1,3} – 2 _{1,2}	9782.3011±0.002	9782.3002±0.0003	0.0009	1
1 _{1,1} – 0 _{0,0}	9923.2290±0.002	9923.2320±0.0008	-0.0030	1
3 _{0,3} – 2 _{0,2}	10236.0247±0.002	10236.0231±0.0003	0.0016	1
3 _{2,1} – 2 _{2,0}	10333.8478±0.002	10333.8506±0.0003	-0.0028	1
3 _{1,2} – 2 _{1,1}	10772.2630±0.002	10772.2641±0.0004	-0.0011	1
2 _{1,2} – 1 _{0,1}	13021.4616±0.002	13021.4612±0.0009	0.0004	1
4 _{1,4} – 3 _{1,3}	13029.4062±0.002	13029.4049±0.0004	0.0013	1
4 _{0,4} – 3 _{0,3}	13591.6516±0.002	13591.6512±0.0004	0.0004	1
4 _{2,3} – 3 _{2,2}	13703.6639±0.002	13703.6635±0.0004	0.0004	1
4 _{3,2} – 3 _{3,1}	13736.7971±0.002	13736.7980±0.0008	-0.0009	1
4 _{3,1} – 3 _{3,0}	13738.5067±0.002	13738.5064±0.0008	0.0003	1
4 _{2,2} – 3 _{2,1}	13825.2872±0.002	13825.2873±0.0004	-0.0001	1
4 _{1,3} – 3 _{1,2}	14348.0230±0.002	14348.0245±0.0005	-0.0015	1
5 _{1,5} – 4 _{1,4}	16265.6263±0.002	16265.6259±0.0004	0.0005	1
5 _{0,5} – 4 _{0,4}	16901.2787±0.002	16901.2786±0.0004	0.0001	1
5 _{2,4} – 4 _{2,3}	17114.2495±0.002	17114.2489±0.0005	0.0007	1
5 _{2,3} – 4 _{2,2}	17354.5142±0.002	17354.5150±0.0005	-0.0008	1
5 _{1,4} – 4 _{1,3}	17910.0601±0.002	17910.0614±0.0005	-0.0013	1
6 _{1,6} – 5 _{1,5}	19489.2327±0.002	19489.2329±0.0005	-0.0002	1
6 _{0,6} – 5 _{0,5}	20158.1916±0.002	20158.1912±0.0005	0.0004	1
6 _{2,5} – 5 _{2,4}	20514.6554±0.002	20514.6529±0.0007	0.0025	1
6 _{2,4} – 5 _{2,3}	20926.1530±0.002	20926.1532±0.0008	-0.0002	1
6 _{1,5} – 5 _{1,4}	21453.8466±0.002	21453.8466±0.0006	0.0000	1
7 _{0,7} – 6 _{0,6}	23360.7767±0.002	23360.7759±0.0006	0.0008	1
7 _{1,6} – 6 _{1,5}	24974.1324±0.002	24974.1330±0.0008	-0.0006	1
9 _{1,8} – 8 _{1,7}	31919.2940±0.020	31919.2920±0.0016	0.0020	2
10 _{1,10} – 9 _{1,9}	32243.7210±0.015	32243.7383±0.0024	-0.0173	2
10 _{2,9} – 9 _{2,8}	33976.6110±0.010	33976.6075±0.0027	0.0035	2
10 _{1,9} – 9 _{1,8}	35330.1070±0.010	35330.0961±0.0022	0.0109	2
11 _{1,11} – 10 _{1,10}	35398.9380±0.020	35398.9204±0.0034	0.0176	2
11 _{0,11} – 10 _{0,10}	35781.5250±0.010	35781.5254±0.0033	-0.0004	2
12 _{1,12} – 11 _{1,11}	38542.8770±0.015	38542.8772±0.0048	-0.0002	2
11 _{1,10} – 10 _{1,9}	38690.1250±0.015	38690.1393±0.0029	-0.0143	2
11 _{2,9} – 10 _{2,8}	39210.1480±0.020	39210.1666±0.0054	-0.0186	2
12 _{2,11} – 11 _{2,10}	40601.4280±0.020	40601.4505±0.0047	-0.0225	2
13 _{0,13} – 12 _{0,12}	41910.8700±0.015	41910.8654±0.0064	0.0046	2
12 _{1,11} – 11 _{1,10}	41993.4530±0.025	41993.4358±0.0039	0.0172	2
12 _{2,10} – 11 _{2,9}	42860.7410±0.015	42860.7280±0.0069	0.0130	2
14 _{1,13} – 13 _{1,12}	48420.1880±0.015	48420.2025±0.0068	-0.0145	2

Notes.^(a) Observed line frequencies and assigned uncertainties.^(b) Calculated frequencies and uncertainties.^(c) Observed-minus-calculated frequencies.^(l) Laboratory data from McCarthy et al. (2020).⁽²⁾ Frequencies observed in TMC-1 assuming a ν_{LSR} of 5.83 km s⁻¹.

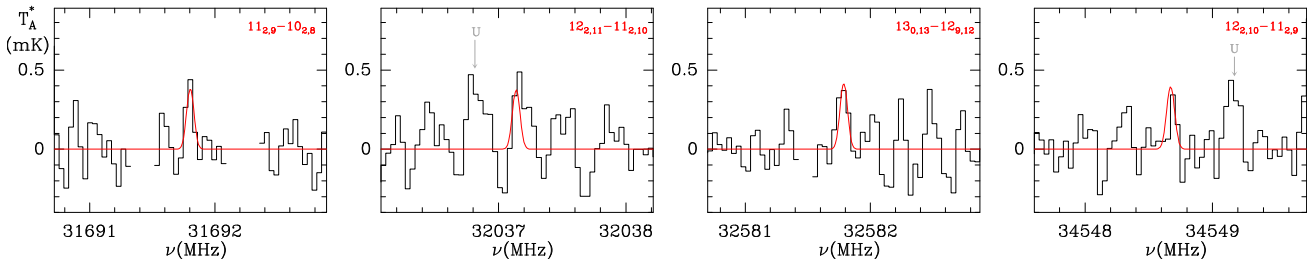


Fig. A.2. Four lines of *EBZ* (C_6H_5CCH) observed in the 31–50 GHz frequency range towards TMC-1. The abscissa corresponds to the rest frequency assuming a local standard of rest velocity of 5.83 km s^{-1} . The ordinate is the antenna temperature corrected for atmospheric and telescope losses in mK. The red line shows the synthetic spectrum obtained from a fit to the observed line profiles adopting a rotational temperature of 9 K, which provides $N(EBZ) = (2.5 \pm 0.4) \times 10^{12} \text{ cm}^{-2}$ (see Sect. 3.2). The rotational quantum numbers are indicated in each panel. Blanked channels correspond to negative features produced in the folding of the frequency switching data.

Appendix A.2: Ethynyl benzene

For *EBZ*, the searched lines are given in Table A.6. Only four lines appear at the 3σ level and are shown in Fig. A.2. The estimated column density is discussed in Sect. 3.2.

Table A.6. Observed line parameters of *EBZ* (ethynyl benzene).

Transition ($J_{K_a, K_c})_u - (J_{K_a, K_c})_l$	ν_{pred}^a (MHz)	ν_{LSR}^b (kms s ⁻¹)	$\int T_A^* dv^c$ (mK km s ⁻¹)	Δv^d (km s ⁻¹)	T_A^{*e} (mK)	N
11 _{2,9} – 10 _{2,8}	31691.804±0.001	5.91±0.09	0.29±0.08	0.58±0.16	0.47±0.15	
12 _{2,11} – 11 _{2,10}	32037.138±0.001	5.73±0.19	0.30±0.10	0.52±0.30	0.54±0.15	
13 _{1,13} – 12 _{1,12}	32505.867±0.001				≤0.54	
13 _{0,13} – 12 _{0,12}	32581.787±0.001	5.93±0.12	0.37±0.09	0.85±0.22	0.41±0.15	
12 _{1,11} – 11 _{1,10}	32988.304±0.001				≤0.50	
12 _{2,10} – 11 _{2,9}	34548.672±0.001	5.63±0.15	0.18±0.06	0.47±0.17	0.37±0.14	
13 _{2,12} – 12 _{2,11}	34570.607±0.001					A
14 _{1,14} – 13 _{1,13}	34926.745±0.001				≤0.66	
14 _{0,14} – 13 _{0,13}	34977.526±0.001				≤0.51	
13 _{1,12} – 12 _{1,11}	35391.232±0.001				≤0.48	
14 _{2,13} – 13 _{2,12}	37081.142±0.001				≤0.44	
15 _{1,15} – 14 _{1,14}	37343.953±0.001				≤0.40	
13 _{2,11} – 12 _{2,10}	37344.487±0.001				≤0.40	
15 _{0,15} – 14 _{0,14}	37377.435±0.001				≤0.55	
14 _{1,13} – 13 _{1,12}	37756.431±0.001				≤0.60	
15 _{2,14} – 14 _{2,13}	39570.906±0.001				≤0.54	
16 _{1,16} – 15 _{1,15}	39758.590±0.001				≤0.48	
16 _{0,16} – 15 _{0,15}	39780.407±0.001				≤0.65	B
14 _{2,12} – 13 _{2,11}	40070.665±0.001				≤0.62	C
15 _{1,14} – 14 _{1,13}	40103.212±0.001				≤0.56	D
16 _{2,15} – 15 _{2,14}	42042.517±0.001				≤0.69	E
17 _{1,17} – 16 _{1,16}	42171.467±0.001				≤0.66	
17 _{0,17} – 16 _{0,16}	42185.545±0.001				≤0.60	
16 _{1,15} – 15 _{1,14}	42446.821±0.001				≤0.60	
15 _{2,13} – 14 _{2,12}	42719.693±0.001				≤0.60	
17 _{2,16} – 16 _{2,15}	44498.814±0.001				≤0.60	
18 _{1,18} – 17 _{1,17}	44583.166±0.001				≤0.60	
18 _{0,18} – 17 _{0,17}	44592.174±0.001				≤0.60	
17 _{1,16} – 16 _{1,15}	44796.545±0.001				≤0.60	
16 _{2,14} – 15 _{2,13}	45286.973±0.001				≤0.60	
18 _{2,17} – 17 _{2,16}	46942.629±0.001				≤0.60	
19 _{1,19} – 18 _{1,18}	46994.089±0.001				≤0.60	
19 _{0,19} – 18 _{0,18}	46999.812±0.001				≤0.60	
18 _{1,17} – 17 _{1,16}	47156.405±0.001				≤0.60	
17 _{2,15} – 16 _{2,14}	47773.527±0.001				≤0.60	
19 _{2,18} – 18 _{2,17}	49376.600±0.001				≤0.60	
20 _{0,20} – 19 _{0,19}	49408.126±0.001				≤0.60	

Notes.

For the observational parameters we adopted the uncertainty of the Gaussian fit provided by GILDAS. Upper limits correspond to 3σ values.

^(a) Predicted frequency from the rotational and distortion constants derived from a fit to the lines observed by Cox et al. (1975), Dreizler et al. (2004), and Kisiel & Krašnicki (2010) (see Sect. 3.2).

^(b) Observed ν_{LSR} in km s⁻¹.

^(c) Integrated line intensity in mK km s⁻¹.

^(d) Line width at half intensity derived by fitting a Gaussian function to the observed line profile (in km s⁻¹).

^(e) Antenna temperature in millikelvin.

^(A) Fully blended with a negative feature produced in the folding of the frequency switching data.

^(B) Partially blended with a unknown feature at 39780.350 MHz. Fit unreliable.

^(C) Partially blended with a unknown feature at 40070.716 MHz. Fit unreliable.

^(D) Partially blended with a unknown feature at 40103.150 MHz. Fit unreliable.

^(E) Partially blended with a unknown feature at 42042.460 MHz. Fit unreliable.

Appendix B: Observed lines of the two isomers of cyano cyclopentadiene (1-CCP and 2-CCP)

Two isomers of cyano cyclopentadiene, 1-CCP and 2-CCP, have been observed in the laboratory by different authors (Ford & Seitzman, 1978; Sakaizumi et al., 1987; McCarthy et al., 2020). The structure of these two isomers is similar to those of 1-ECP and 2-ECP when the CCH group is changed by CN (see Fig. 1). Dipole moments for both species were measured by Ford & Seitzman (1978) and Sakaizumi et al. (1987), who provided values of $\mu_a=4.15\pm0.15$ and 4.36 ± 0.25 D for 1-CCP and 2-CCP, respectively. Transitions of *b* type are expected to be much weaker due to the measured low value of the dipole moment along the *b* axis of 0.27 and 0.77 D, respectively (Sakaizumi et al., 1987).

The accuracy of the measurements in McCarthy et al. (2020) is much higher than those of the early microwave measurements of the two isomers, and their rotational and distortion constants, improved by additional measurements by Lee et al. (2021), were used to predict their frequencies in the domain of our QUIJOTE line survey. The two isomers were detected through stacking techniques towards TMC-1 by McCarthy et al. (2021) and Lee et al. (2021). However, as mentioned in Sect. 3.3 and below, the column densities they provide are rather uncertain, with a variation for N(1-CCP) of a factor of four between both publications. In order to provide a coherent set of column densities for the ethynyl and cyano derivatives of cyclopentadiene and benzene, we analysed their lines within our survey.

For 1-CCP, the published laboratory frequencies of McCarthy et al. (2020) cover the range 7.3-29.9 GHz, with $J_{max}=9$ and $K_a \leq 3$. The rotational constants provided by Lee et al. (2021) were derived with unpublished frequencies up to 36 GHz and provide frequency predictions for the 31-50 GHz domain with uncertainties ≤ 15 kHz. We observed 47 lines of 1-CCP with QUIJOTE, and their line parameters are given in Table B.1. Selected lines for 1-CCP are shown in Fig. B.1. The red and blue lines in Fig. B.1 show the synthetic spectrum for a column density of $3.1 \times 10^{11} \text{ cm}^{-2}$ and rotational temperatures of 9 and 6 K, respectively. It is clear, as it is robustly derived for benzonitrile in Appendix C, that the rotational temperature has to be close to 9 K in order to fit the observed parameters for lines arising from levels with $K_a=3-4$. A fit to the observed line profiles, assuming a source diameter of $80''$ (Fossé et al., 2001), provides $T_{rot}=9.0\pm1.0$ K and $N(1-CCP)=(3.1\pm0.3)\times10^{11} \text{ cm}^{-2}$. The lines shown in Fig. B.1 that involve energy levels below 10 K can be fitted with a rotational temperature of 6 K with practically the same column density, a fact that has been discussed for other species by Cernicharo et al. (2021e); it arises from the small dependence of the line opacity with T_{rot} for these transitions as well as from the balance between the term $[T_{rot} - 2.7]$ and the partition function, which is proportional to T_{rot} for linear molecules and to $T_{rot}^{3/2}$ for asymmetric species. Only with observations that provide a reasonable range of upper level energies for the lines is it possible to derive an accurate rotational temperature and a reliable column density.

McCarthy et al. (2021) reported for 1-CCP a rotational temperature of 6.0 ± 0.3 K and a total column density of $(1.44\pm0.17)\times10^{12} \text{ cm}^{-2}$. However, Lee et al. (2021) revised these values, also using spectral data stacking, and derive a rotational temperature of 6.00 ± 0.03 K and a total column density of $(8.27\pm0.10)\times10^{11} \text{ cm}^{-2}$ for the same isomer (i.e. a factor of three larger than our estimation and a factor of 1.7 lower than in McCarthy et al. 2021). Lee et al. (2021) argue that they used a larger partition function for 1-CCP than McCarthy et al. (2021), resulting in a substantially lower column density for this isomer. However, the effect should be the opposite as the column density is proportional to the partition function and to the rotational temperature, which is the same in both studies. The difference in the column density between both works is probably due to the highest data sensitivity in the Lee et al. (2021) analysis. Their results correspond to a fit to four velocity components with different spatial sizes. The lack of individual lines, together with the limited spatial coverage of their data (a single position with all information on spatial sizes arising from the beam size variation with frequency), renders the fit rather optimistic, and many of the derived parameters may be strongly correlated. The lack of spatial information also applies to the QUIJOTE data. However, a rotational temperature as low as 6 K cannot explain our 47 observed lines as shown in Fig. B.1. Although the stacking procedure is a powerful method for extracting information from spectral data below the noise level, the determination of physical parameters from line stacking has to be done with extreme caution. The determination of the column density and rotational temperature of 1-CCP by McCarthy et al. (2021) and Lee et al. (2021) seems to be a bit optimistic given their small quoted uncertainties. The differences between the values determined in this work and their studies could be related to the adopted source diameter and to the beam size of both telescopes.

For 2-CCP, the laboratory frequencies measured by McCarthy et al. (2020) cover the range 7.3-18.1 GHz, with $J_{max}=5$ and $K_a \leq 2$; hence, the predictions in the frequency domain 31-50 GHz could be more uncertain than those of 1-CCP. The derived line parameters for all the detected lines of 2-CCP are given in Table B.2, and the lines are shown in Fig. B.2. Differences between predicted and observed frequencies reach values as high as 100 kHz. However, using the rotational and distortion constants of Lee et al. (2021), the differences between predicted and observed frequencies never exceed 20 kHz. The range of energies covered by our observations is not large enough to allow a fit to the rotational temperature, and we adopted the value derived for 1-CCP (9 K). The derived column density for 2-CCP is $(1.3\pm0.2)\times10^{11}$, a value 1.5 times lower than that of Lee et al. (2021). Hence, the abundance ratio between 1-CCP and 2-CCP, derived from a significant number of lines for each isomer, is ~ 2.4 , a factor of two lower than the ratio derived by Lee et al. (2021).

We used the observed line frequencies in TMC-1 and those of the laboratory (McCarthy et al., 2020) to improve the rotational and distortion constants for both isomers (see Appendix B.1).

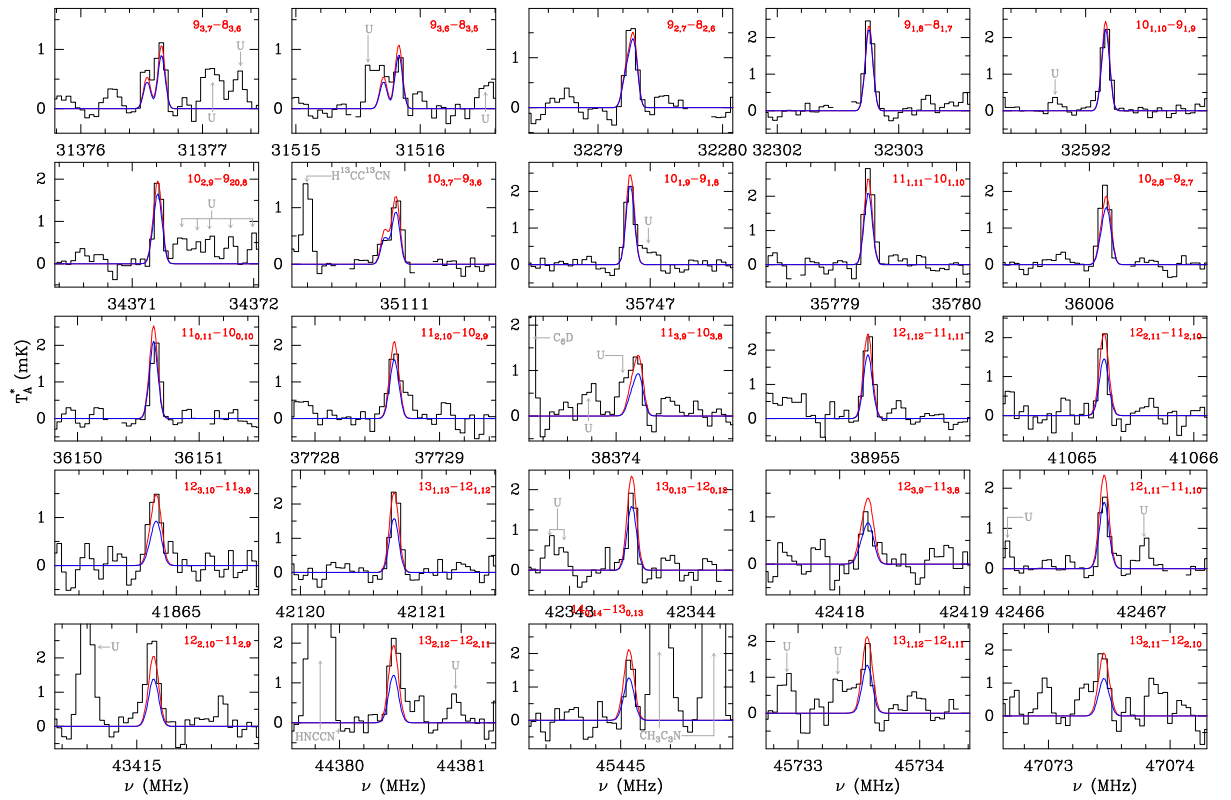


Fig. B.1. Selected lines of 1-CCP in the 31-50 GHz frequency range towards TMC-1. The abscissa corresponds to the rest frequency assuming a local standard of rest velocity of 5.83 km s^{-1} . The ordinate is the antenna temperature corrected for atmospheric and telescope losses in mK. The red line shows the synthetic spectrum obtained from a fit to the observed line profiles, which provides $T_{rot} = 9.0 \pm 1.0 \text{ K}$ and $N(1\text{-CCP}) = (3.1 \pm 0.3) \times 10^{11} \text{ cm}^{-2}$ (see Appendix B). The blue line shows the synthetic spectrum for the same column density and a rotational temperature of 6 K. The rotational quantum numbers are indicated in each panel. Blanked channels correspond to negative features produced in the folding of the frequency switching data.

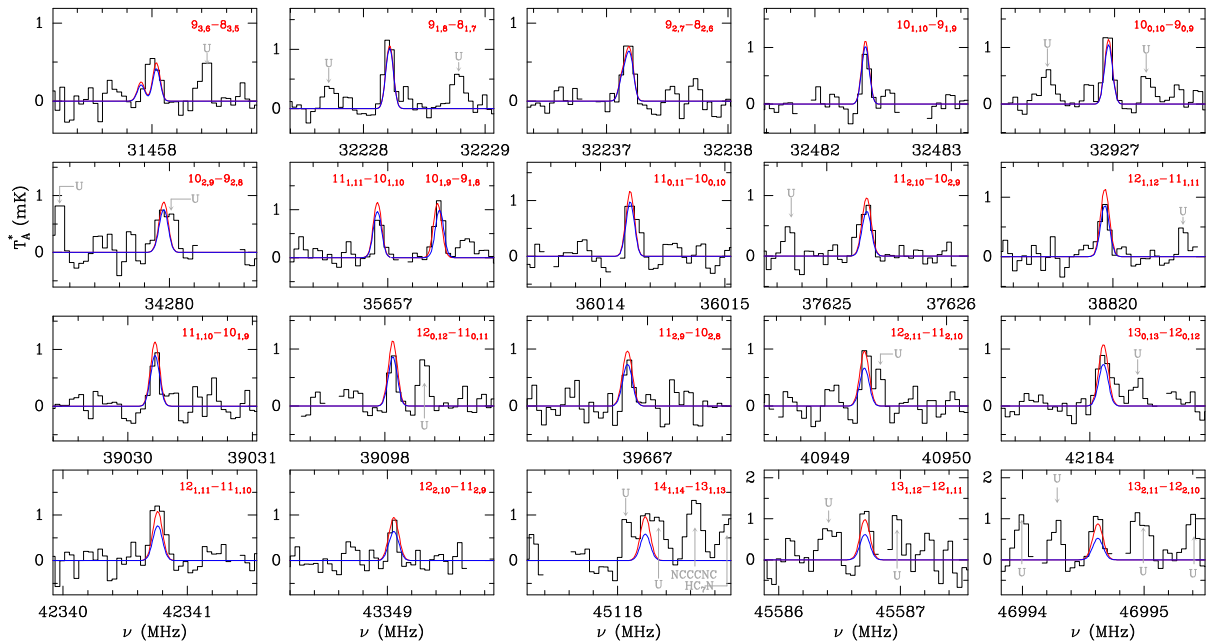


Fig. B.2. Observed lines of 2-CCP in the 31-50 GHz frequency range towards TMC-1. The abscissa corresponds to the rest frequency assuming a local standard of rest velocity of 5.83 km s^{-1} . The ordinate is the antenna temperature corrected for atmospheric and telescope losses in mK. The red line shows the synthetic spectrum obtained from a fit to the observed line profiles, which provides $N(2\text{-CCP}) = (1.3 \pm 0.2) \times 10^{11} \text{ cm}^{-2}$ for a rotational temperature of 9 K. (see Appendix B). The blue line shows the synthetic spectrum for the same column density and a rotational temperature of 6 K. The rotational quantum numbers are indicated in each panel. Blanked channels correspond to negative features produced in the folding of the frequency switching data.

Table B.1. Observed lines of 1-CCP towards TMC-1.

Transition ($J_{K_a,K_c})_u - (J_{K_a,K_c})_l$	ν_{pred}^a (MHz)	ν_{obs}^b (MHz)	$\int T_A^* d\nu^c$ (mK km s ⁻¹)	$\Delta\nu^d$ (km s ⁻¹)	$T_A^* e$ (mK)	Notes
9 _{4,6} – 8 _{4,5}	31348.548±0.003				≤0.62	A
9 _{4,5} – 8 _{4,4}	31353.423±0.003	31353.504±0.010	0.40±0.09	0.66±0.13	0.57±0.15	
9 _{3,7} – 8 _{3,6} $F = 9 - 8$	31376.544±0.002	31376.560±0.010	0.37±0.05	0.42±0.25	0.85±0.16	
..... $F = 10 - 9 + F = 8 - 7$	31376.661±0.002	31376.653±0.010	1.27±0.06	1.06±0.12	1.11±0.16	
9 _{3,6} – 8 _{3,5} $F = 9 - 8$	31515.698±0.002	31515.689±0.020	0.36±0.10	0.54±0.30	0.62±0.16	
..... $F = 10 - 9 + F = 8 - 7$	31515.821±0.002	31515.833±0.010	0.52±0.14	0.57±0.15	0.86±0.16	
9 _{2,7} – 8 _{2,6}	32279.259±0.003	32279.265±0.010	1.68±0.12	0.90±0.07	1.75±0.16	
9 _{1,8} – 8 _{1,7}	32302.755±0.003	32302.755±0.010	2.14±0.13	0.80±0.06	2.51±0.16	
10 _{1,10} – 9 _{1,9}	32592.160±0.003	32592.161±0.010	1.92±0.11	0.79±0.06	2.30±0.15	
10 _{0,10} – 9 _{0,9}	33050.463±0.003	33050.408±0.020	4.35±0.03	1.45±0.04	2.80±0.15	B
10 _{2,9} – 9 _{2,8}	34371.215±0.005	34371.214±0.010	1.33±0.08	0.63±0.04	2.00±0.14	
10 _{4,7} – 9 _{4,6} $F = 10 - 9$	34856.901±0.004					C
..... $F = 11 - 10 + F = 9 - 8$	34857.055±0.004	34857.062±0.010	0.43±0.07	0.47±0.15	0.86±0.14	D
10 _{4,6} – 9 _{4,5}	34867.504±0.006				≤0.54	A
10 _{3,8} – 9 _{3,7} $F = 10 - 9$	34877.024±0.003	34877.049±0.020	0.34±0.12	0.64±0.31	0.50±0.15	
..... $F = 11 - 10 + F = 9 - 8$	34877.109±0.003	34877.177±0.020	1.04±0.25	1.54±0.39	0.64±0.15	E
10 _{3,7} – 9 _{3,6} $F = 10 - 9$	35110.827±0.003	35110.822±0.015	0.36±0.11	0.84±0.33	0.40±0.16	
..... $F = 9 - 8 + F = 11 - 10$	35110.919±0.003	35110.936±0.010	1.00±0.13	0.79±0.10	1.19±0.16	
10 _{1,9} – 9 _{1,8}	35746.835±0.004	35746.834±0.010	1.67±0.14	0.73±0.07	2.16±0.15	
11 _{1,11} – 10 _{1,10}	35779.275±0.004	35779.278±0.010	2.23±0.12	0.74±0.05	2.88±0.17	
10 _{2,8} – 9 _{2,7}	36006.125±0.005	36006.124±0.010	1.92±0.12	0.80±0.05	2.24±0.16	
11 _{0,11} – 10 _{0,10}	36150.641±0.004	36150.642±0.010	1.60±0.11	0.71±0.06	2.13±0.18	
11 _{2,10} – 10 _{2,9}	37728.644±0.007	37728.647±0.010	2.09±0.18	1.19±0.15	1.64±0.17	E
11 _{4,8} – 10 _{4,7} $F = 11 - 10$	38372.076±0.004	38372.043±0.030	0.25±0.11	0.66±0.24	0.36±0.16	
..... $F = 12 - 11 + F = 10 - 9$	38372.191±0.004	38372.194±0.015	1.16±0.14	0.82±0.13	1.33±0.16	
11 _{3,9} – 10 _{3,8} $F = 11 - 10$	38374.124±0.005	38374.103±0.020	0.42±0.10	0.55±0.25	0.67±0.16	
..... $F = 10 - 9 + F = 12 - 11$	38374.188±0.005	38374.179±0.010	0.85±0.14	0.65±0.25	1.35±0.16	
11 _{4,7} – 10 _{4,6} $F = 11 - 10$	38392.912±0.004				≤0.55	A
..... $F = 12 - 11 + F = 10 - 9$	38393.029±0.004	38393.027±0.015	0.54±0.10	0.55±0.13	0.93±0.18	
11 _{3,8} – 10 _{3,7} $F = 11 - 10$	38743.577±0.005	38743.566±0.030	0.43±0.12	0.51±0.15	0.69±0.18	
..... $F = 10 - 9 + F = 12 - 11$	38743.648±0.005	38743.651±0.030	0.70±0.13	0.54±0.11	1.20±0.18	
12 _{1,12} – 11 _{1,11}	38954.943±0.005	38954.947±0.010	1.80±0.14	0.67±0.06	2.52±0.18	
11 _{1,10} – 10 _{1,9}	39136.812±0.005	39136.808±0.010	1.43±0.14	0.62±0.07	2.16±0.17	
12 _{0,12} – 11 _{0,11}	39246.342±0.005	39246.342±0.010	1.54±0.40	0.52±0.17	2.76±0.60	F
11 _{2,9} – 10 _{2,8}	39722.554±0.006	39722.563±0.015	0.66±0.12	0.43±0.08	1.41±0.21	D
12 _{2,11} – 11 _{2,10}	41065.272±0.010	41065.255±0.010	1.31±0.17	0.53±0.08	2.33±0.22	
12 _{3,10} – 11 _{3,9}	41864.830±0.007	41864.824±0.010	1.46±0.19	0.92±0.15	1.48±0.23	E
12 _{4,9} – 11 _{4,8}	41893.726±0.005				≤0.69	A
12 _{4,8} – 11 _{4,7}	41932.390±0.005				≤0.69	A
13 _{1,13} – 12 _{1,12}	42120.773±0.007	42120.781±0.010	1.69±0.13	0.63±0.06	2.51±0.18	
13 _{0,13} – 12 _{0,12}	42343.514±0.007	42343.516±0.010	1.15±0.15	0.51±0.08	2.12±0.21	
12 _{3,9} – 11 _{3,8}	42418.202±0.007	42418.209±0.025	0.67±0.20	0.55±0.17	1.14±0.24	
12 _{1,11} – 11 _{1,10}	42466.697±0.007	42466.693±0.010	1.17±0.11	0.59±0.07	1.86±0.17	
12 _{2,10} – 11 _{2,9}	43415.138±0.008	43415.121±0.010	2.33±0.19	0.87±0.09	2.51±0.21	
13 _{2,12} – 12 _{2,11}	44380.459±0.013	44380.458±0.010	1.82±0.20	0.82±0.12	2.10±0.21	
14 _{1,14} – 13 _{1,13}	45278.391±0.010	45278.405±0.015	0.70±0.14	0.46±0.09	1.43±0.27	
13 _{3,11} – 12 _{3,10}	45345.911±0.009				≤0.81	A
13 _{4,10} – 12 _{4,9}	45421.042±0.007				≤0.81	A
14 _{0,14} – 13 _{0,13}	45445.085±0.010	45445.076±0.010	1.11±0.16	0.52±0.08	1.99±0.31	
13 _{4,9} – 12 _{4,8}	45488.849±0.007				≤0.94	A
13 _{1,12} – 12 _{1,11}	45733.576±0.010	45733.564±0.015	0.85±0.23	0.44±0.09	1.79±0.29	
13 _{3,10} – 12 _{3,9}	46135.659±0.011	46135.650±0.020	0.88±0.22	0.62±0.18	1.32±0.36	
13 _{2,11} – 12 _{2,10}	47073.451±0.010	47073.438±0.020	1.32±0.29	0.62±0.14	2.02±0.38	
14 _{2,13} – 13 _{2,12}	47674.019±0.016	47674.018±0.020	1.51±0.28	0.98±0.25	1.45±0.35	

Notes.

For the observational parameters we adopted the uncertainty of the Gaussian fit provided by GILDAS.

Upper limits correspond to 3σ values.

^(a) Predictions based on the rotational constants of Lee et al. (2021) (see also McCarthy et al. 2020, Sect. 3.3).

^(b) Observed frequency assuming a v_{LSR} of 5.83 km s⁻¹.

^(c) Integrated line intensity in mK km s⁻¹.

^(d) Line width at half intensity derived by fitting a Gaussian function to the observed line profile (in km s⁻¹).

^(e) Antenna temperature in millikelvin.

^(A) Below the detection limit. ^(B) Blended with the $J_K = 8_2 - 7_2$ line of CH₃C₃N. ^(C) See next entry. ^(D) Affected by a negative feature produced in the folding of the frequency switching data. ^(E) Broad line due to the hyperfine structure of the transition. ^(F) Noisy zone of the spectrum.

Table B.2. Observed lines of 2-CCP towards TMC-1.

Transition ($J_{K_a, K_c})_u - (J_{K_a, K_c})_l$	ν_{pred}^a (MHz)	ν_{obs}^b (MHz)	$\int T_A^* dv^c$ (mK km s ⁻¹)	Δv^d (km s ⁻¹)	T_A^{*e} (mK)	Notes
9 _{3,6} – 8 _{3,5}	31457.995±0.006	31458.005±0.010	0.69±0.13	1.12±0.23	0.57±0.14	E
9 _{1,8} – 8 _{1,7}	32228.215±0.006	32228.207±0.010	1.08±0.13	0.85±0.09	1.20±0.12	
9 _{2,7} – 8 _{2,6}	32237.173±0.006	32237.180±0.010	0.76±0.10	0.89±0.13	0.80±0.12	
10 _{1,10} – 9 _{1,9}	32482.415±0.009	32482.420±0.010	0.62±0.10	0.60±0.12	0.97±0.16	
10 _{0,10} – 9 _{0,9}	32926.951±0.009	32926.946±0.010	0.95±0.12	0.71±0.11	1.26±0.16	
10 _{2,9} – 9 _{2,8}	34279.918±0.009	34279.970±0.020	1.21±0.19	1.44±0.23	0.79±0.19	E
11 _{1,11} – 10 _{1,10}	35656.918±0.011	35656.932±0.010	0.57±0.08	0.60±0.11	0.89±0.13	
10 _{1,9} – 9 _{1,8}	35657.417±0.008	35657.412±0.010	0.95±0.08	0.73±0.07	1.20±0.13	
10 _{2,8} – 9 _{2,7}	35958.391±0.007					D
11 _{0,11} – 10 _{0,10}	36014.223±0.012	36014.255±0.010	0.98±0.26	0.85±0.15	1.00±0.14	
11 _{2,10} – 10 _{2,9}	37625.343±0.012	37625.308±0.015	0.96±0.13	0.88±0.13	0.83±0.18	
12 _{1,12} – 11 _{1,11}	38819.937±0.014	38819.928±0.010	0.68±0.12	0.75±0.18	0.85±0.16	
11 _{1,10} – 10 _{1,9}	39030.219±0.011	39030.222±0.010	0.61±0.11	0.58±0.14	1.00±0.18	
12 _{0,12} – 11 _{0,11}	39098.064±0.014	39098.060±0.010	0.50±0.09	0.49±0.10	0.95±0.18	
11 _{2,9} – 10 _{2,8}	39666.839±0.009	39666.848±0.015	0.49±0.11	0.54±0.13	0.86±0.20	
12 _{2,11} – 11 _{2,10}	40949.324±0.015	40949.339±0.015	0.62±0.11	0.54±0.12	1.08±0.18	
13 _{1,13} – 12 _{1,12}	41973.156±0.017					D
13 _{0,13} – 12 _{0,12}	42184.094±0.017	42184.110±0.030	0.39±0.10	0.64±0.18	0.57±0.17	
12 _{1,11} – 11 _{1,10}	42340.761±0.015	42340.761±0.010	1.29±0.15	0.86±0.11	1.32±0.20	
12 _{2,10} – 11 _{2,9}	43349.053±0.011	43349.049±0.015	0.44±0.11	0.42±0.13	0.99±0.22	
14 _{1,14} – 13 _{1,13}	45118.255±0.021	45118.232±0.030	0.97±0.26	0.95±0.38	0.96±0.24	
14 _{0,14} – 13 _{0,13}	45274.919±0.021					D
13 _{1,12} – 12 _{1,11}	45586.689±0.019	45586.714±0.020	0.72±0.17	0.54±0.12	1.25±0.32	
13 _{2,11} – 12 _{2,10}	46994.644±0.014	46994.606±0.020	1.07±0.17	0.70±0.11	1.44±0.28	

Notes.

For the observational parameters we adopted the uncertainty of the Gaussian fit provided by GILDAS.

(^a) Predictions based on the rotational constants of Lee et al. (2021) (see also McCarthy et al. 2020, Sect. 3.3).

(^b) Observed frequency assuming a v_{LSR} of 5.83 km s⁻¹.

(^c) Integrated line intensity in mK km s⁻¹.

(^d) Line width at half intensity derived by fitting a Gaussian function to the observed line profile (in km s⁻¹).

(^e) Antenna temperature in millikelvin.

(^D) Affected by a negative feature produced in the folding of the frequency switching data. (^E) Broad line due to the hyperfine structure of the transition.

Table B.3. Molecular constants for 1-CCP and 2-CCP.

Constant	1-CCP ^a (MHz)	1-CCP ^b (MHz)	2-CCP ^a (MHz)	2-CCP ^b (MHz)
<i>A</i>	8352.981(10)	8352.9758(142)	8235.592(14)	8235.599(37)
<i>B</i>	1904.2522(2)	1904.251830(231)	1902.0748(3)	1902.07558(49)
<i>C</i>	1565.3652(2)	1565.365658(197)	1559.6472(2)	1559.64673(38)
$\Delta_J 10^{-3}$	0.0743(11)	0.07280(110)	0.0686(11)	0.07246(240)
$\Delta_{JK} 10^{-3}$	2.354(8)	2.3493(134)	2.287(21)	2.248(37)
$\Delta_K 10^{-3}$	0.17561 ^c		0.32391 ^c	
$\delta_J 10^{-5}$	1.33(5)	1.320(52)	1.34(6)	1.465(82)
$\delta_K 10^{-3}$	1.48(9)	1.322(81)	1.10(9)	1.299(191)
χ_{aa}	-4.1810(11)	-4.1795 (23)	-4.2429(6)	-4.2316 (55)
χ_{bb}	2.3016(14)	2.3052 (38)	2.2475(16)	2.2347 (74)
<i>N</i> _{lines}	68	175	38	98
<i>v</i> _{max} (GHz)	29.9	47.6	18.1	47.0
(<i>J</i> , <i>K</i> _a) _{max}	9,3	14,3	5,2	13,2
σ (kHz)	2.2	9.1	1.9	10.3

Notes.

Values between parentheses correspond to the uncertainties of the parameters in units of the last significant digits.

^(a) Rotational and distortion constants from Lee et al. (2021).

^(b) Merged fit to the laboratory data of McCarthy et al. (2020) and space frequencies measured in this work. The laboratory data used by Lee et al. (2021) are not available.

^(c) Fixed value.

Appendix B.1: Improved rotational constants for 1-CCP and 2-CCP

The observed lines of 1-CCP (see Table B.1) and 2-CCP (see Table B.2) were merged with the laboratory data (McCarthy et al., 2020) to provide a new set of rotational and distortion constants. They are given in Table B.3 and can be used to predict the frequencies of the rotational transitions for the two observed isomers of cyano cyclopentadiene up to 50 GHz with an accuracy better than 15 kHz ($K_a \leq 3$). The calculated and the observed-minus-calculated frequencies for 1-CCP and 2-CCP are given in Tables B.4 and B.5, respectively.

Table B.4. Observed and calculated line frequencies for 1-CCP.

J'	K'_a	K'_c	J''	K''_a	K''_c	F'	F''	ν_{obs}^a (MHz)	ν_{calc}^b (MHz)	$\nu_{obs} - \nu_{calc}^c$ (MHz)	Notes
2	0	2	2	1	0	1	2	6924.9737	6924.9753	-0.0016	1
2	0	2	1	1	0	1	0	6925.1742	6925.1768	-0.0026	1
2	0	2	2	1	0	1	1	6926.2273	6926.2290	-0.0017	1
2	0	2	3	1	0	1	2	6926.3145	6926.3138	0.0008	1
2	0	2	1	1	0	1	1	6928.3108	6928.3114	-0.0006	1
2	1	1	2	1	1	0	1	7277.0535	7277.0592	-0.0057	1
2	1	1	2	1	1	0	2	7277.6180	7277.6212	-0.0032	1
2	1	1	3	1	1	0	2	7278.3608	7278.3621	-0.0013	1
3	1	3	3	2	1	2	3	9891.6689	9891.6697	-0.0008	1
3	1	3	3	2	1	2	2	9892.2695	9892.2721	-0.0026	1
3	1	3	4	2	1	2	3	9892.6421	9892.6412	0.0009	1
3	1	3	2	2	1	2	2	9893.5811	9893.5838	-0.0027	1
3	0	3	2	2	0	2	1	10356.7289	10356.7293	-0.0004	1
3	0	3	3	2	0	2	2	10356.9498	10356.9478	0.0020	1
3	0	3	4	2	0	2	3	10356.9901	10356.9899	0.0002	1
3	2	2	3	2	2	1	2	10407.7424	10407.7435	-0.0011	1
3	2	2	3	2	2	1	2	10407.7424	10407.7435	-0.0011	1
3	2	2	4	2	2	1	3	10409.0876	10409.0868	0.0008	1
3	2	1	4	2	2	0	3	10460.9891	10460.9913	-0.0022	1
3	2	1	2	2	2	0	1	10461.7333	10461.7395	-0.0062	1
3	1	2	3	2	1	1	3	10907.8578	10907.8588	-0.0010	1
3	1	2	3	2	1	1	2	10908.5994	10908.5997	-0.0003	1
3	1	2	2	2	1	1	1	10908.9552	10908.9522	0.0030	1
3	1	2	4	2	1	1	3	10908.9747	10908.9738	0.0009	1
3	1	2	2	2	1	1	2	10910.1016	10910.1052	-0.0036	1
4	1	4	4	3	1	3	3	13175.4738	13175.4710	0.0028	1
4	1	4	3	3	1	3	2	13175.5840	13175.5847	-0.0007	1
4	1	4	5	3	1	3	4	13175.6334	13175.6333	0.0001	1
4	0	4	3	3	0	3	2	13749.4229	13749.4239	-0.0010	1
4	0	4	4	3	0	3	3	13749.5243	13749.5253	-0.0010	1
4	0	4	5	3	0	3	4	13749.5483	13749.5467	0.0016	1
4	2	3	4	3	2	2	3	13867.8420	13867.8411	0.0010	1
4	2	3	5	3	2	2	4	13868.4103	13868.4098	0.0005	1
4	2	3	3	3	2	2	2	13868.5578	13868.5559	0.0019	1
4	2	2	5	3	2	1	4	13997.3397	13997.3399	-0.0002	1
4	1	3	4	3	1	2	3	14529.1170	14529.1160	0.0010	1
4	1	3	3	3	1	2	2	14529.2191	14529.2201	-0.0010	1
4	1	3	5	3	1	2	4	14529.2828	14529.2812	0.0016	1
5	1	5	5	4	1	4	4	16447.0681	16447.0680	0.0002	1
5	1	5	4	4	1	4	3	16447.1112	16447.1120	-0.0008	1
5	1	5	6	4	1	4	5	16447.1543	16447.1549	-0.0006	1
5	0	5	4	4	0	4	3	17093.4579	17093.4567	0.0012	1
5	0	5	5	4	0	4	4	17093.5202	17093.5204	-0.0002	1
5	0	5	6	4	0	4	5	17093.5326	17093.5297	0.0029	1
5	1	4	5	4	1	3	4	18134.9211	18134.9206	0.0005	1
5	1	4	4	4	1	3	3	18134.9593	18134.9586	0.0007	1
5	1	4	6	4	1	3	5	18135.0103	18135.0091	0.0012	1
7	1	7	7	6	1	6	6	22949.1633	22949.1652	-0.0019	1
7	1	7	6	6	1	6	5	22949.1747	22949.1721	0.0026	1
7	1	7	8	6	1	6	7	22949.1989	22949.1986	0.0003	1
7	0	7	6	6	0	6	5	23614.2508	23614.2463	0.0045	1
7	0	7	8	6	0	6	7	23614.2823	23614.2827	-0.0004	1
7	0	7	7	6	0	6	6	23614.2823	23614.2827	-0.0004	1
7	2	6	7	6	2	5	6	24186.1313	24186.1327	-0.0014	1
7	2	6	6	6	2	5	5	24186.2294	24186.2342	-0.0048	1
7	2	6	8	6	2	5	7	24186.2469	24186.2438	0.0031	1
7	3	5	8	6	3	4	7	24376.3271	24376.3310	-0.0039	1
7	3	5	6	6	3	4	5	24376.3571	24376.3529	0.0042	1
7	2	5	7	6	2	4	6	24858.3337	24858.3276	0.0061	1
7	2	5	6	6	2	4	5	24858.4414	24858.4448	-0.0034	1
7	2	5	8	6	2	4	7	24858.4555	24858.4535	0.0020	1
7	1	6	7	6	1	5	6	25282.4392	25282.4374	0.0018	1
7	1	6	6	6	1	5	5	25282.4392	25282.4374	0.0018	1
7	1	6	8	6	1	5	7	25282.4669	25282.4688	-0.0019	1
8	0	8	9	7	0	7	8	26795.3336	26795.3363	-0.0027	1
8	0	8	8	7	0	7	7	26795.3336	26795.3363	-0.0027	1
9	0	9	10	8	0	8	9	29936.2435	29936.2433	0.0002	1
9	0	9	9	8	0	8	8	29936.2435	29936.2433	0.0002	1
9	4	5	10	8	4	4	9	31353.5040	31353.4899	0.0141	2
9	3	7	9	8	3	6	8	31376.5600	31376.5447	0.0153	2
9	3	7	8	8	3	6	7	31376.6530	31376.6626	-0.0096	2
9	3	7	10	8	3	6	9	31376.6530	31376.6626	-0.0096	2
9	3	6	9	8	3	5	8	31515.6890	31515.7012	-0.0122	2

Table B.4. continued.

J'	K'_a	K'_c	J''	K''_a	K''_c	F'	F''	ν_{obs}^a (MHz)	ν_{calc}^b (MHz)	$\nu_{obs} - \nu_{calc}^c$ (MHz)	Notes
9	3	6	10	8	3	5	9	31515.8330	31515.8239	0.0091	2
9	3	6	8	8	3	5	7	31515.8330	31515.8239	0.0091	2
9	2	7	8	8	2	6	7	32279.2650	32279.2797	-0.0147	2
9	2	7	10	8	2	6	9	32279.2650	32279.2797	-0.0147	2
9	1	8	8	8	1	7	7	32302.7550	32302.7514	0.0036	2
9	1	8	9	8	1	7	8	32302.7550	32302.7514	0.0036	2
9	1	8	10	8	1	7	9	32302.7550	32302.7514	0.0036	2
10	1	10	9	9	1	9	8	32592.1610	32592.1611	-0.0001	2
10	1	10	10	9	1	9	9	32592.1610	32592.1611	-0.0001	2
10	1	10	11	9	1	9	10	32592.1610	32592.1611	-0.0001	2
10	0	10	9	9	0	9	8	33050.4080	33050.4633	-0.0553	2
10	0	10	11	9	0	9	10	33050.4080	33050.4633	-0.0553	2
10	0	10	10	9	0	9	9	33050.4080	33050.4633	-0.0553	2
10	2	9	10	9	2	8	9	34371.2140	34371.2105	0.0035	2
10	2	9	9	9	2	8	8	34371.2140	34371.2105	0.0035	2
10	2	9	11	9	2	8	10	34371.2140	34371.2105	0.0035	2
10	4	7	9	9	4	6	8	34857.0620	34857.0623	-0.0003	2
10	3	8	10	9	3	7	9	34877.0490	34877.0243	0.0247	2
10	3	7	10	9	3	6	9	35110.8220	35110.8305	-0.0085	2
10	3	7	9	9	3	6	8	35110.9360	35110.9222	0.0138	2
10	3	7	11	9	3	6	10	35110.9360	35110.9222	0.0138	2
10	1	9	9	9	1	8	8	35746.8340	35746.8311	0.0029	2
10	1	9	10	9	1	8	9	35746.8340	35746.8311	0.0029	2
10	1	9	11	9	1	8	10	35746.8340	35746.8311	0.0029	2
11	1	11	10	10	1	10	9	35779.2780	35779.2760	0.0020	2
11	1	11	11	10	1	10	10	35779.2780	35779.2760	0.0020	2
11	1	11	12	10	1	10	11	35779.2780	35779.2760	0.0020	2
10	2	8	10	9	2	7	9	36006.1240	36006.1266	-0.0026	2
10	2	8	9	9	2	7	8	36006.1240	36006.1266	-0.0026	2
10	2	8	11	9	2	7	10	36006.1240	36006.1266	-0.0026	2
11	0	11	10	10	0	10	9	36150.6420	36150.6422	-0.0002	2
11	0	11	12	10	0	10	11	36150.6420	36150.6422	-0.0002	2
11	0	11	11	10	0	10	10	36150.6420	36150.6422	-0.0002	2
11	2	10	11	10	2	9	10	37728.6470	37728.6388	0.0083	2
11	2	10	10	10	2	9	9	37728.6470	37728.6388	0.0083	2
11	2	10	12	10	2	9	11	37728.6470	37728.6388	0.0083	2
11	4	8	11	10	4	7	10	38372.0430	38372.0795	-0.0365	2
11	4	8	12	10	4	7	11	38372.1940	38372.1952	-0.0012	2
11	4	8	10	10	4	7	9	38372.1940	38372.1952	-0.0012	2
11	3	9	11	10	3	8	10	38374.1030	38374.1238	-0.0208	2
11	3	9	10	10	3	8	9	38374.1790	38374.1874	-0.0084	2
11	3	9	12	10	3	8	11	38374.1790	38374.1874	-0.0084	2
11	4	7	12	10	4	6	11	38393.0270	38393.0330	-0.0060	2
11	4	7	10	10	4	6	9	38393.0270	38393.0330	-0.0060	2
11	3	8	11	10	3	7	10	38743.5660	38743.5819	-0.0159	2
11	3	8	10	10	3	7	9	38743.6510	38743.6535	-0.0025	2
11	3	8	12	10	3	7	11	38743.6510	38743.6535	-0.0025	2
12	1	12	11	11	1	11	10	38954.9470	38954.9446	0.0024	2
12	1	12	12	11	1	11	11	38954.9470	38954.9446	0.0024	2
12	1	12	13	11	1	11	12	38954.9470	38954.9446	0.0024	2
11	1	10	10	10	1	9	9	39136.8080	39136.8067	0.0013	2
11	1	10	11	10	1	9	10	39136.8080	39136.8067	0.0013	2
11	1	10	12	10	1	9	11	39136.8080	39136.8067	0.0013	2
12	0	12	11	11	0	11	10	39246.3420	39246.3437	-0.0017	2
12	0	12	13	11	0	11	12	39246.3420	39246.3437	-0.0017	2
12	0	12	12	11	0	11	11	39246.3420	39246.3437	-0.0017	2
11	2	9	11	10	2	8	10	39722.5630	39722.5548	0.0082	2
11	2	9	10	10	2	8	9	39722.5630	39722.5548	0.0082	2
11	2	9	12	10	2	8	11	39722.5630	39722.5548	0.0082	2
12	2	11	12	11	2	10	11	41065.2550	41065.2652	-0.0102	2
12	2	11	11	11	2	10	10	41065.2550	41065.2652	-0.0102	2
12	2	11	13	11	2	10	12	41065.2550	41065.2652	-0.0102	2
12	3	10	12	11	3	9	11	41864.8240	41864.8275	-0.0035	2
12	3	10	11	11	3	9	10	41864.8240	41864.8275	-0.0035	2
12	3	10	13	11	3	9	12	41864.8240	41864.8275	-0.0035	2
13	1	13	12	12	1	12	11	42120.7810	42120.7758	0.0052	2
13	1	13	13	12	1	12	12	42120.7810	42120.7758	0.0052	2
13	1	13	14	12	1	12	13	42120.7810	42120.7758	0.0052	2
13	0	13	12	12	0	12	11	42343.5160	42343.5164	-0.0004	2
13	0	13	14	12	0	12	13	42343.5160	42343.5164	-0.0004	2
13	0	13	13	12	0	12	12	42343.5160	42343.5164	-0.0004	2
12	3	9	12	11	3	8	11	42418.2090	42418.2075	0.0015	2
12	3	9	11	11	3	8	10	42418.2090	42418.2075	0.0015	2
12	3	9	13	11	3	8	12	42418.2090	42418.2075	0.0015	2

Table B.4. continued.

J'	K'_a	K'_c	J''	K''_a	K''_c	F'	F''	ν_{obs}^a (MHz)	ν_{calc}^b (MHz)	$\nu_{obs} - \nu_{calc}^c$ (MHz)	Notes
12	1	11	11	11	1	10	10	42466.6930	42466.6895	0.0035	2
12	1	11	13	11	1	10	12	42466.6930	42466.6895	0.0035	2
12	1	11	12	11	1	10	11	42466.6930	42466.6895	0.0035	2
12	2	10	12	11	2	9	11	43415.1210	43415.1388	-0.0178	2
12	2	10	11	11	2	9	10	43415.1210	43415.1388	-0.0178	2
12	2	10	13	11	2	9	12	43415.1210	43415.1388	-0.0178	2
13	2	12	13	12	2	11	12	44380.4580	44380.4491	0.0089	2
13	2	12	12	12	2	11	11	44380.4580	44380.4491	0.0089	2
13	2	12	14	12	2	11	13	44380.4580	44380.4491	0.0089	2
14	1	14	13	13	1	13	12	45278.4050	45278.3947	0.0103	2
14	1	14	14	13	1	13	13	45278.4050	45278.3947	0.0103	2
14	1	14	15	13	1	13	14	45278.4050	45278.3947	0.0103	2
14	0	14	13	13	0	13	12	45445.0760	45445.0882	-0.0122	2
14	0	14	15	13	0	13	14	45445.0760	45445.0882	-0.0122	2
14	0	14	14	13	0	13	13	45445.0760	45445.0882	-0.0122	2
13	1	12	12	12	1	11	11	45733.5640	45733.5666	-0.0026	2
13	1	12	14	12	1	11	13	45733.5640	45733.5666	-0.0026	2
13	1	12	13	12	1	11	12	45733.5640	45733.5666	-0.0026	2
13	3	10	13	12	3	9	12	46135.6500	46135.6655	-0.0155	2
13	3	10	12	12	3	9	11	46135.6500	46135.6655	-0.0155	2
13	3	10	14	12	3	9	13	46135.6500	46135.6655	-0.0155	2
13	2	11	13	12	2	10	12	47073.4380	47073.4511	-0.0131	2
13	2	11	12	12	2	10	11	47073.4380	47073.4511	-0.0131	2
13	2	11	14	12	2	10	13	47073.4380	47073.4511	-0.0131	2
14	2	13	14	13	2	12	13	47674.0180	47674.0074	0.0106	2
14	2	13	13	13	2	12	12	47674.0180	47674.0074	0.0106	2
14	2	13	15	13	2	12	14	47674.0180	47674.0074	0.0106	2

Notes.^(a) Observed line frequencies and assigned uncertainties.^(b) Calculated frequencies and uncertainties.^(c) Observed-minus-calculated frequencies.⁽¹⁾ Laboratory data from McCarthy et al. (2020).⁽²⁾ Frequencies observed in TMC-1 assuming a v_{LSR} of 5.83 km s⁻¹.

Table B.5. Observed and calculated line frequencies for 2-CCP.

J'	K'_a	K'_c	J''	K''_a	K''_c	F'	F''	ν_{obs}^a (MHz)	ν_{calc}^b (MHz)	$\nu_{obs} - \nu_{calc}^c$ (MHz)	Notes
2	1	1	3	1	1	0	2	7266.1158	7266.1160	-0.0002	1
3	1	3	3	2	1	2	3	9862.3228	9862.3225	0.0003	1
3	1	3	3	2	1	2	2	9862.9633	9862.9643	-0.0010	1
3	1	3	4	2	1	2	3	9863.3416	9863.3396	0.0020	1
3	1	3	2	2	1	2	2	9864.3366	9864.3377	-0.0011	1
3	0	3	2	2	0	2	1	10331.0354	10331.0363	-0.0009	1
3	0	3	3	2	0	2	2	10331.2534	10331.2546	-0.0012	1
3	0	3	4	2	0	2	3	10331.2998	10331.2996	0.0002	1
3	2	2	3	2	2	1	2	10384.0499	10384.0474	0.0025	1
3	2	2	4	2	2	1	3	10385.4117	10385.4074	0.0043	1
3	1	2	3	2	1	1	2	10889.8976	10889.8986	-0.0010	1
3	1	2	2	2	1	1	1	10890.2582	10890.2612	-0.0030	1
3	1	2	4	2	1	1	3	10890.2772	10890.2767	0.0005	1
4	1	4	3	3	1	3	2	13135.9674	13135.9701	-0.0027	1
4	1	4	5	3	1	3	4	13136.0237	13136.0221	0.0016	1
4	1	4	3	3	1	3	3	13137.3441	13137.3436	0.0005	1
4	0	4	3	3	0	3	2	13712.9093	13712.9081	0.0012	1
4	0	4	4	3	0	3	3	13713.0091	13713.0071	0.0020	1
4	0	4	5	3	0	3	4	13713.0319	13713.0319	0.0000	1
4	2	3	4	3	2	2	3	13835.8635	13835.8654	-0.0019	1
4	2	3	5	3	2	2	4	13836.4421	13836.4416	0.0005	1
4	2	3	3	3	2	2	2	13836.5882	13836.5897	-0.0015	1
4	2	2	4	3	2	1	3	13969.7215	13969.7222	-0.0007	1
4	2	2	5	3	2	1	4	13970.3043	13970.3056	-0.0013	1
4	2	2	3	3	2	1	2	13970.4531	13970.4547	-0.0016	1
4	1	3	4	3	1	2	3	14503.5437	14503.5444	-0.0007	1
4	1	3	3	3	1	2	2	14503.6554	14503.6529	0.0025	1
4	1	3	5	3	1	2	4	14503.7120	14503.7117	0.0003	1
5	1	5	5	4	1	4	4	16396.7422	16396.7420	0.0002	1
5	1	5	4	4	1	4	3	16396.7864	16396.7864	0.0000	1
5	1	5	6	4	1	4	5	16396.8316	16396.8315	0.0002	1
5	1	5	4	4	1	4	4	16398.2745	16398.2737	0.0008	1
5	0	5	4	4	0	4	3	17044.4234	17044.4268	-0.0034	1
5	0	5	5	4	0	4	4	17044.4853	17044.4869	-0.0016	1
5	0	5	6	4	0	4	5	17044.5023	17044.5003	0.0020	1
5	1	4	5	4	1	3	4	18101.8650	18101.8636	0.0014	1
5	1	4	4	4	1	3	3	18101.9048	18101.9045	0.0003	1
5	1	4	6	4	1	3	5	18101.9544	18101.9537	0.0007	1
9	3	6	9	8	3	5	8	31458.0050	31457.9951	0.0099	2
9	3	6	10	8	3	5	9	31458.0050	31457.9951	0.0099	2
9	3	6	8	8	3	5	7	31458.0050	31457.9951	0.0099	2
9	1	8	8	8	1	7	7	32228.2070	32228.2150	-0.0080	2
9	1	8	9	8	1	7	8	32228.2070	32228.2150	-0.0080	2
9	1	8	10	8	1	7	9	32228.2070	32228.2150	-0.0080	2
9	2	7	8	8	2	6	7	32237.1800	32237.1870	-0.0070	2
9	2	7	10	8	2	6	9	32237.1800	32237.1870	-0.0070	2
10	1	10	9	9	1	9	8	32482.4200	32482.4148	0.0052	2
10	1	10	10	9	1	9	9	32482.4200	32482.4148	0.0052	2
10	1	10	11	9	1	9	10	32482.4200	32482.4148	0.0052	2
10	0	10	9	9	0	9	8	32926.9460	32926.9508	-0.0048	2
10	0	10	10	9	0	9	9	32926.9460	32926.9508	-0.0048	2
10	2	9	10	9	2	8	9	34279.9700	34279.9239	0.0461	2
10	2	9	9	9	2	8	8	34279.9700	34279.9239	0.0461	2
10	2	9	11	9	2	8	10	34279.9700	34279.9239	0.0461	2
11	1	11	10	10	1	10	9	35656.9320	35656.9174	0.0146	2
11	1	11	11	10	1	10	10	35656.9320	35656.9174	0.0146	2
11	1	11	12	10	1	10	11	35656.9320	35656.9174	0.0146	2
10	1	9	9	9	1	8	8	35657.4120	35657.4171	-0.0051	2
10	1	9	10	9	1	8	9	35657.4120	35657.4171	-0.0051	2
10	1	9	11	9	1	8	10	35657.4120	35657.4171	-0.0051	2
11	0	11	11	10	0	10	10	36014.2550	36014.2229	0.0321	2
11	2	10	11	10	2	9	10	37625.3080	37625.3501	-0.0421	2
11	2	10	10	10	2	9	9	37625.3080	37625.3501	-0.0421	2
11	2	10	12	10	2	9	11	37625.3080	37625.3501	-0.0421	2
12	1	12	11	11	1	11	10	38819.9280	38819.9366	-0.0086	2
12	1	12	12	11	1	11	11	38819.9280	38819.9366	-0.0086	2
12	1	12	13	11	1	11	12	38819.9280	38819.9366	-0.0086	2
11	1	10	10	10	1	9	9	39030.2220	39030.2201	0.0019	2
11	1	10	11	10	1	9	10	39030.2220	39030.2201	0.0019	2
11	1	10	12	10	1	9	11	39030.2220	39030.2201	0.0019	2
12	0	12	11	11	0	11	10	39098.0600	39098.0636	-0.0036	2
12	0	12	13	11	0	11	12	39098.0600	39098.0636	-0.0036	2

Table B.5. continued.

J'	K'_a	K'_c	J''	K''_a	K''_c	F'	F''	ν_{obs}^a (MHz)	ν_{calc}^b (MHz)	$\nu_{obs} - \nu_{calc}^c$ (MHz)	Notes
12	0	12	12	11	0	11	11	39098.0600	39098.0636	-0.0036	2
11	2	9	11	10	2	8	10	39666.8480	39666.8294	0.0187	2
11	2	9	10	10	2	8	9	39666.8480	39666.8294	0.0187	2
11	2	9	12	10	2	8	11	39666.8480	39666.8294	0.0187	2
12	2	11	12	11	2	10	11	40949.3390	40949.3329	0.0061	2
12	2	11	11	11	2	10	10	40949.3390	40949.3329	0.0061	2
12	2	11	13	11	2	10	12	40949.3390	40949.3329	0.0061	2
13	0	13	12	12	0	12	11	42184.1100	42184.0934	0.0166	2
13	0	13	14	12	0	12	13	42184.1100	42184.0934	0.0166	2
13	0	13	13	12	0	12	12	42184.1100	42184.0934	0.0166	2
12	1	11	11	11	1	10	10	42340.7610	42340.7647	-0.0037	2
12	1	11	13	11	1	10	12	42340.7610	42340.7647	-0.0037	2
12	1	11	12	11	1	10	11	42340.7610	42340.7647	-0.0037	2
12	2	10	12	11	2	9	11	43349.0490	43349.0406	0.0084	2
12	2	10	11	11	2	9	10	43349.0490	43349.0406	0.0084	2
12	2	10	13	11	2	9	12	43349.0490	43349.0406	0.0084	2
14	1	14	15	13	1	13	14	45118.2320	45118.2539	-0.0219	2
13	1	12	12	12	1	11	11	45586.7140	45586.6964	0.0176	2
13	1	12	14	12	1	11	13	45586.7140	45586.6964	0.0176	2
13	1	12	13	12	1	11	12	45586.7140	45586.6964	0.0176	2
13	2	11	13	12	2	10	12	46994.6060	46994.6288	-0.0228	2
13	2	11	12	12	2	10	11	46994.6060	46994.6288	-0.0228	2
13	2	11	14	12	2	10	13	46994.6060	46994.6288	-0.0228	2

Notes.^(a) Observed line frequencies and assigned uncertainties.^(b) Calculated frequencies and uncertainties.^(c) Observed-minus-calculated frequencies.⁽¹⁾ Laboratory data from McCarthy et al. (2020).⁽²⁾ Frequencies observed in TMC-1 assuming a v_{LSR} of 5.83 km s⁻¹.

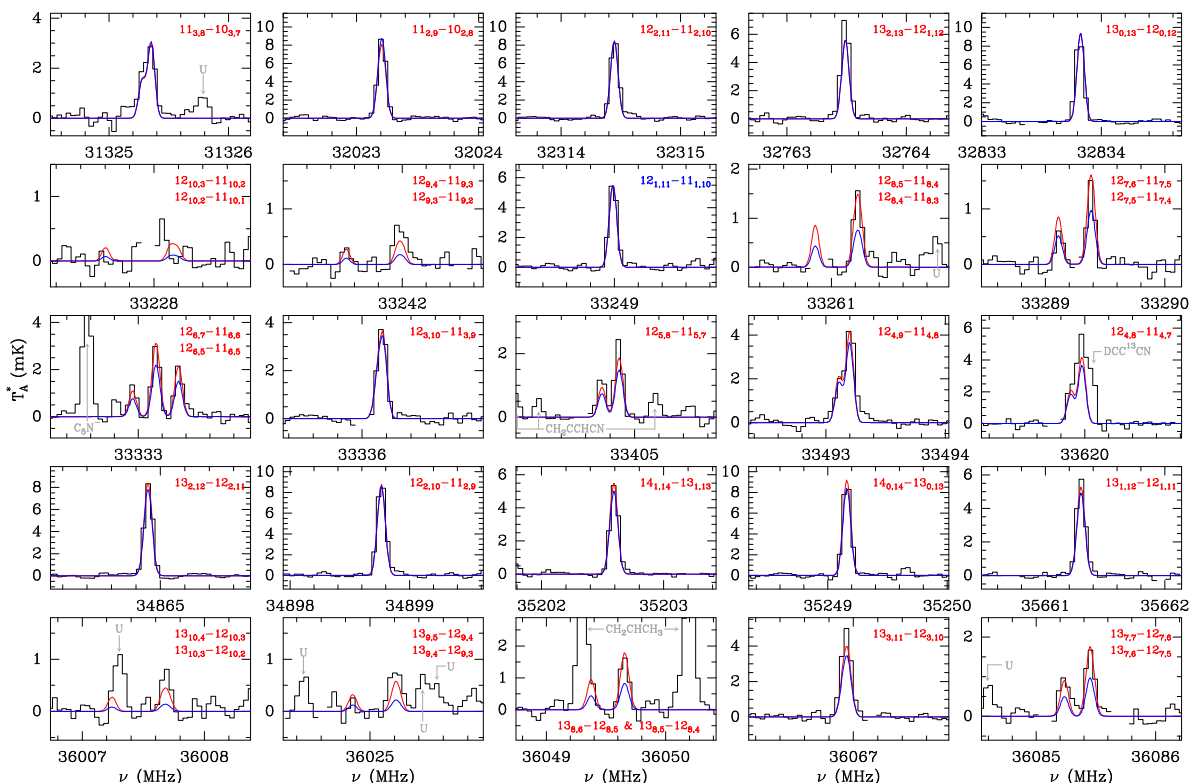


Fig. C.1. Observed lines of C₆H₅CN in the 31-50 GHz frequency range towards TMC-1. The abscissa corresponds to the rest frequency assuming a local standard of rest velocity of 5.83 km s⁻¹. The ordinate is the antenna temperature corrected for atmospheric and telescope losses in mK. The red line shows the synthetic spectrum obtained from a fit to the observed line profiles, which provides $T_r = 9 \pm 0.5$ K and $N(\text{C}_6\text{H}_5\text{CN}) = (1.2 \pm 0.1) \times 10^{12}$ cm⁻². The blue line shows the synthetic spectrum for a rotational temperature of 6 K and a column density of 1.5×10^{12} cm⁻². The rotational quantum numbers are indicated in each panel. Blanked channels correspond to negative features produced in the folding of the frequency switching data. While the blue line produces a very good agreement with the observed intensities for $K_a \leq 4$, for higher values of K_a it underestimates the observed intensities by a factor of two.

Appendix C: Benzonitrile, C₆H₅CN

Benzonitrile, C₆H₅CN, was detected in TMC-1 by McGuire et al. (2018). Assuming a rotational temperature of 7 K, these authors derived a column density of 4×10^{11} cm⁻². In a more recent work by Burkhardt et al. (2021), the total derived column density is 1.6×10^{12} cm⁻² (i.e. a factor of four higher than previously reported), and the derived rotational temperature is 6.1 ± 0.3 K. We explored all lines of benzonitrile in our QUIJOTE line survey. A hundred lines were detected, some of which show hyperfine splitting. They are shown in Figs. C.1, C.2, C.3, and C.4. A fit to the observed lines, assuming the same source parameters as for *ECP* and *CCP*, provides a rotational temperature of 9.0 ± 0.5 K and a column density of $(1.2 \pm 0.1) \times 10^{12}$ cm⁻². The corresponding synthetic spectrum is shown by the red line in these figures. Adopting a lower rotational temperature of 6 K, and maintaining the same column density, we could reproduce the lines reasonably well with $K_a \leq 3$ (blue line in the figures). However, the synthetic line profiles for $T_{\text{rot}} = 6$ K systematically fail to reproduce the lines involving $K_a \geq 4$. Definitely, the rotational temperature has to be close to 9 K (i.e. near the kinetic temperature of the cloud). This result is consistent with the rotational temperatures derived for indene (Cernicharo et al., 2021a) and for the ethynyl and cyano derivatives of cyclopentadiene, as discussed in Sects. 3.1 and 3.3. The small discrepancy between the column densities for benzonitrile derived from GOTHAM (1.6×10^{12} cm⁻²) and QUIJOTE (1.2×10^{12} cm⁻²) data is probably related to the difference in the beam size, the assumed and/or fitted source size, and the rotational temperature used in each set of data for this species.

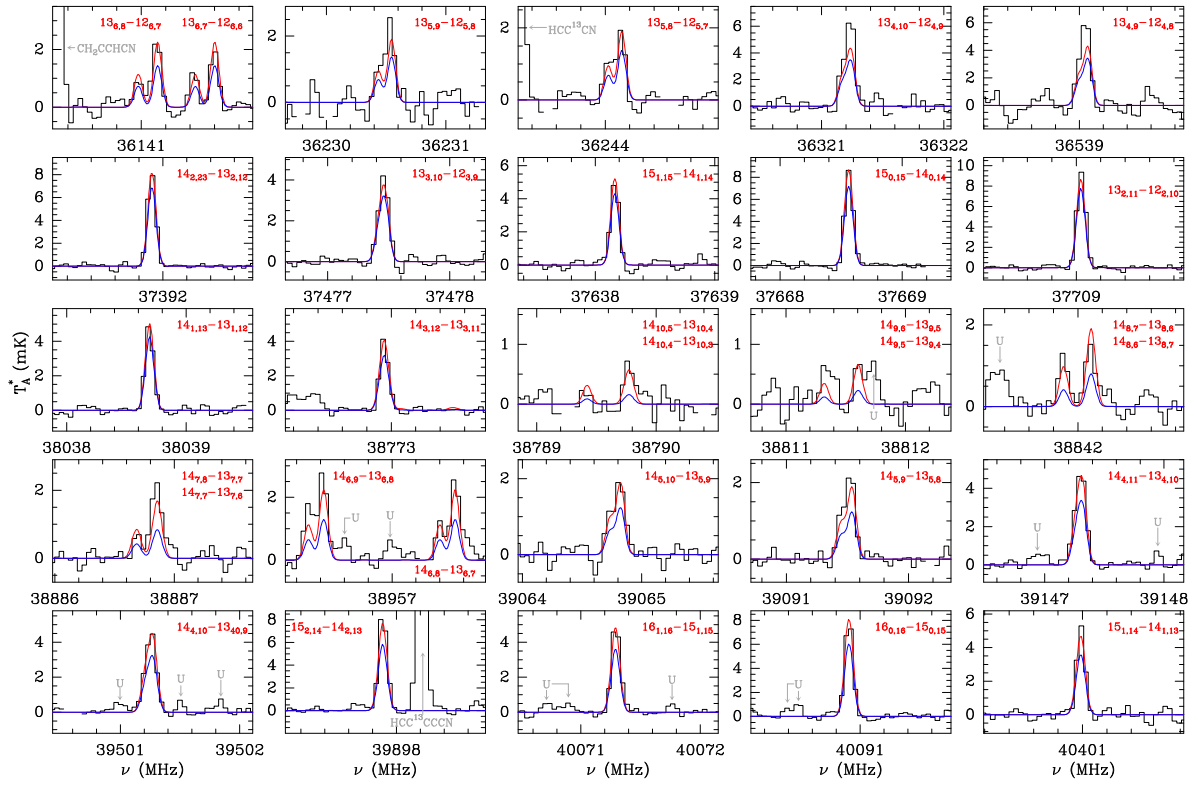


Fig. C.2. Same as Fig. C.1.

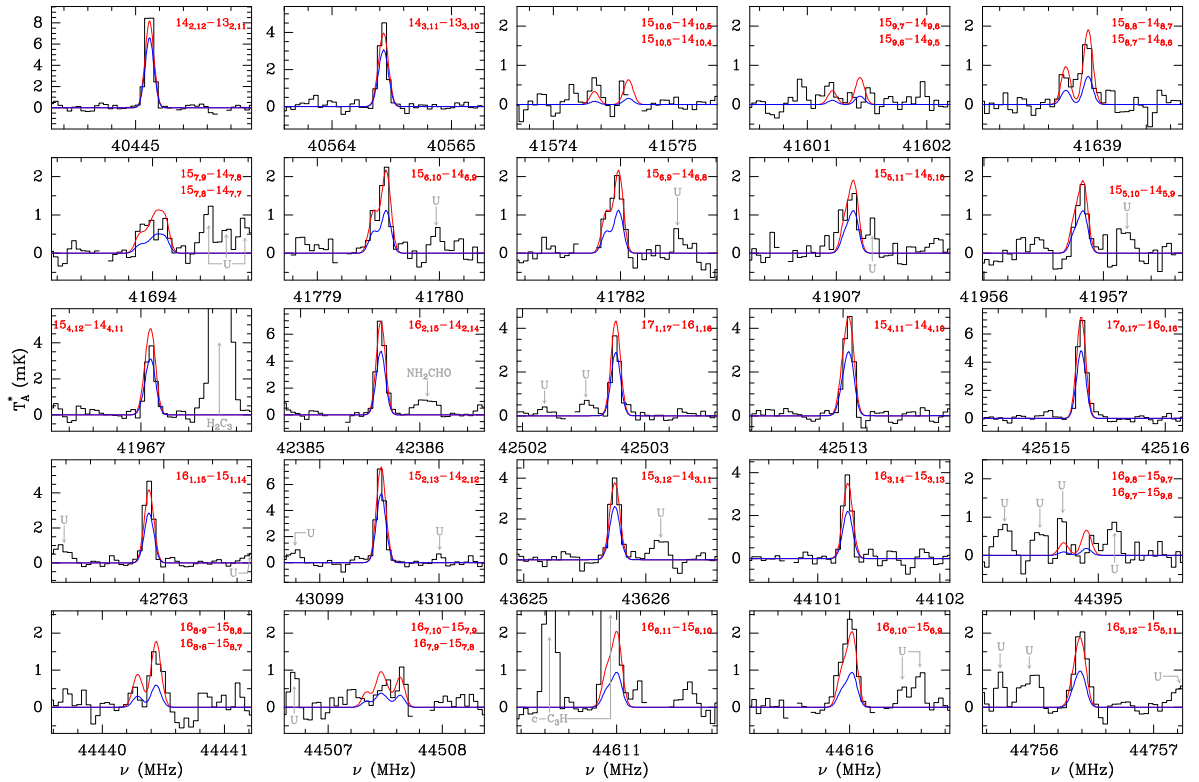


Fig. C.3. Same as Fig. C.1.

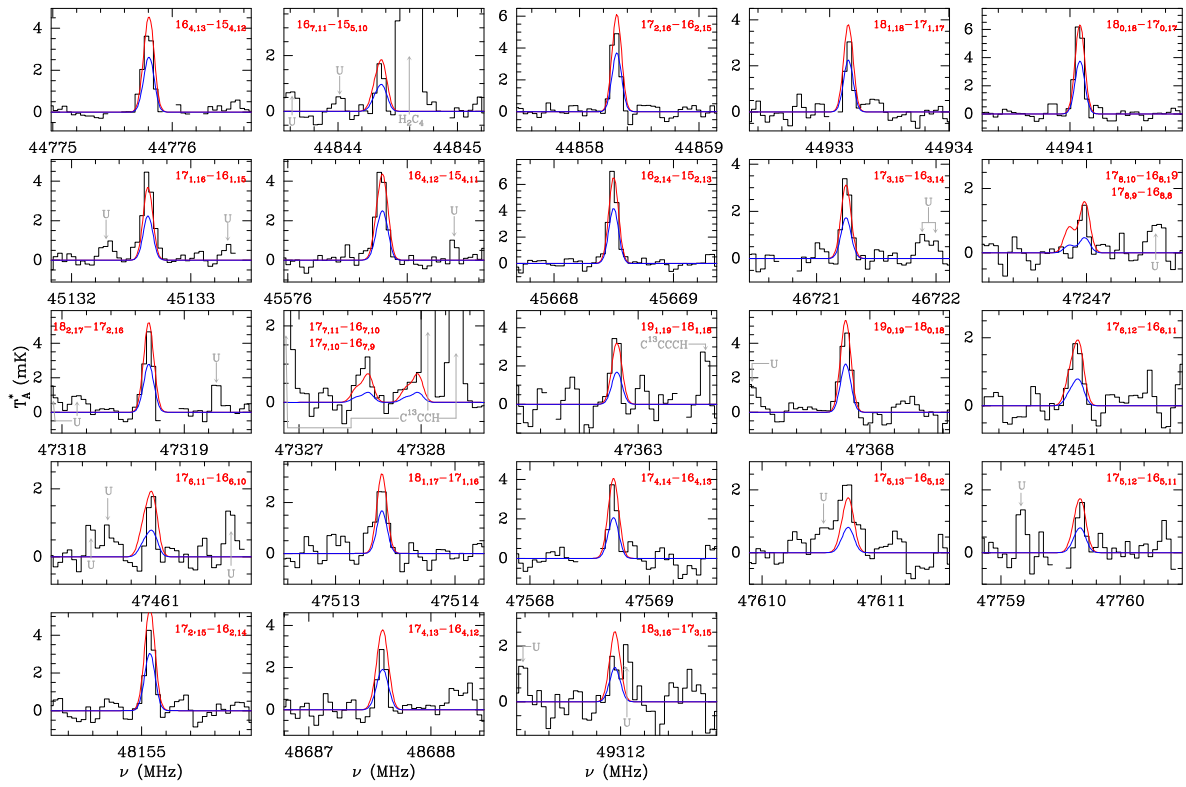
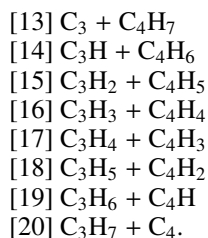
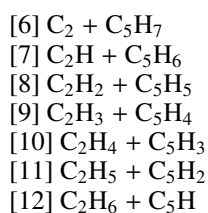
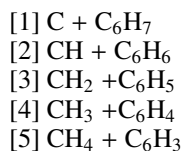


Fig. C.4. Same as Fig. C.1.

Appendix D: Chemical scheme

TMC-1 represents a prototype of a cold molecular cloud, that is, an interstellar environment characterized by low average gas temperatures of about 10 K and number densities of molecular hydrogen ranging from 10^4 to 10^6 cm^{-3} . In the gas phase, these low temperatures and pressures require exoergic bimolecular reactions of the type $A + B \rightarrow C + D$ to proceed without entrance barriers, such as rapid neutral-neutral reactions (Kaiser & Hansen, 2021). With respect to the newly detected 1-*ECP* and 2-*ECP* (labelled as products $p1$ and $p2$ in Fig. D.1), which resemble the product C, and atomic hydrogen as the light counter fragment D, this involves indirect reactions accessing the C_7H_7 potential energy surface. This C_7 hydrocarbon can be formed from the A plus B reactants via bimolecular collisions of C_1 - C_6 , C_2 - C_5 , and C_3 - C_4 hydrocarbon species at various degrees of hydrogenation, as detailed via reactions [1]-[5], [6]-[12], and [13]-[20] (see Fig. D.1):



Among these reactions, multiple bimolecular reactions potentially leading to C_7H_7 isomers plus atomic hydrogen are either direct or follow indirect dynamics with entrance barriers; these processes are therefore closed under the physical conditions in TMC-1. In detail, reaction [5] does not lead to any C_7H_7 isomer since any doublet C_6H_3 radical abstracts a hydrogen atom from the closed shell methane (CH_4) reactant, forming the methyl radical (CH_3) plus C_6H_4 isomers through transition states located between 5 and 30 kJ mol^{-1} above the separated reactants (Kaiser et al. 2011, and therein references). The direct nature and exclusive hydrogen abstraction also prohibit reaction [12] (i.e. C_5H radicals forming ethyl (C_2H_5) radicals plus C_5H_2 isomer), once again through barriers from 5 and 30 kJ mol^{-1} . The remaining reactions are indirect, via C_7H_7 complex formation. Among them, reactions [8]–[10] as well as [16]–[18] involve entrance barriers of addition of the doublet radical to the carbon-carbon double and triple bonds of 90 - 144 kJ mol^{-1} (reaction [8]; da Silva et al. 2010), 8 - 40 kJ mol^{-1} (reactions [9] and [10]), 44 - 130 kJ mol^{-1} for the propargyl radical (C_3H_3) reaction with vinylacetylene (C_4H_4) (reaction [16]; da Silva 2017, and references therein), 8 - 40 kJ mol^{-1} (reaction [17]), and 29 - 104 kJ mol^{-1} for reaction [18] of the allyl radical (C_3H_5) with diacetylene (C_4H_2) (Bodi et al. 2015, and therein references). The remaining reactions have no entrance barriers.

Here, reaction [2] was explored under single-collision conditions in crossed molecular beams as well as computationally (He et al., 2020b). The results reveal a strong energy and hence temperature dependence of the branching ratios with acetylene (C_2H_2) and cyclopentadienyl (C_5H_5) formed almost exclusively at temperatures of 10 K. Both reactions [1] and [3] access the same surface through distinct barrier-less entrance channels of carbon atom addition to the cyclic C_6H_7 radical (reaction [1]) followed by ring opening and/or hydrogen migration of the collision complex and carbene (CH_2)–phenyl radical (C_6H_5) recombination that leads to the benzyl radical ($\text{C}_6\text{H}_5\text{CH}_2$). Although reaction [4] has never been explored experimentally or computationally, a barrier-less methyl (CH_3)–*o*-benzynes (C_6H_4) reaction leads to the *o*-tolyl radical ($\text{C}_6\text{H}_4\text{CH}_3$), which isomerizes through hydrogen shift to the benzyl radical ($\text{C}_6\text{H}_5\text{CH}_2$). These reaction intermediates are coupled to the intermediates accessed through reaction [2]. Consequently, reactions [1]–[4] are not expected to lead to 1-*ECP* and 2-*ECP* isomers ($\text{C}_5\text{H}_5\text{CCH}$).

Reactions of the carbon clusters C_2 , C_3 , and C_4 (reactions [6], [13], and [20]) have not been explored computationally or experimentally. Likewise, the co-reactants C_5H_7 , C_4H_7 , and C_3H_7 have not been included in any astrochemical model. Therefore, the actual effect on the production of 1-*ECP* and 2-*ECP* isomers is unknown. Although reaction [19] is barrier-less and both the propylene (C_3H_6) and butadienyl reactants (C_4H) have been observed in TMC-1, the reaction is not expected to lead to 1-*ECP* and 2-*ECP*. Recent crossed molecular beam and computational studies of the ethynyl (CCH) reaction with propylene (C_3H_6) revealed reaction dynamics dictated by ethynyl addition – hydrogen loss mechanisms, but not to the thermodynamically most stable cyclopentadiene (C_5H_6) isomer (Kaiser and Mebel, in preparation). Since butadienyl (C_4H) is isolobal to ethynyl (CCH) and hence can be considered as an ethynyl-substituted ethynyl radical, the dynamics of reaction [19] are not expected to form 1-*ECP* and 2-*ECP*, but rather butadienyl-substituted propylene isomers. Further, the reactivities of the interstellar *c*- C_3H_2 isomer

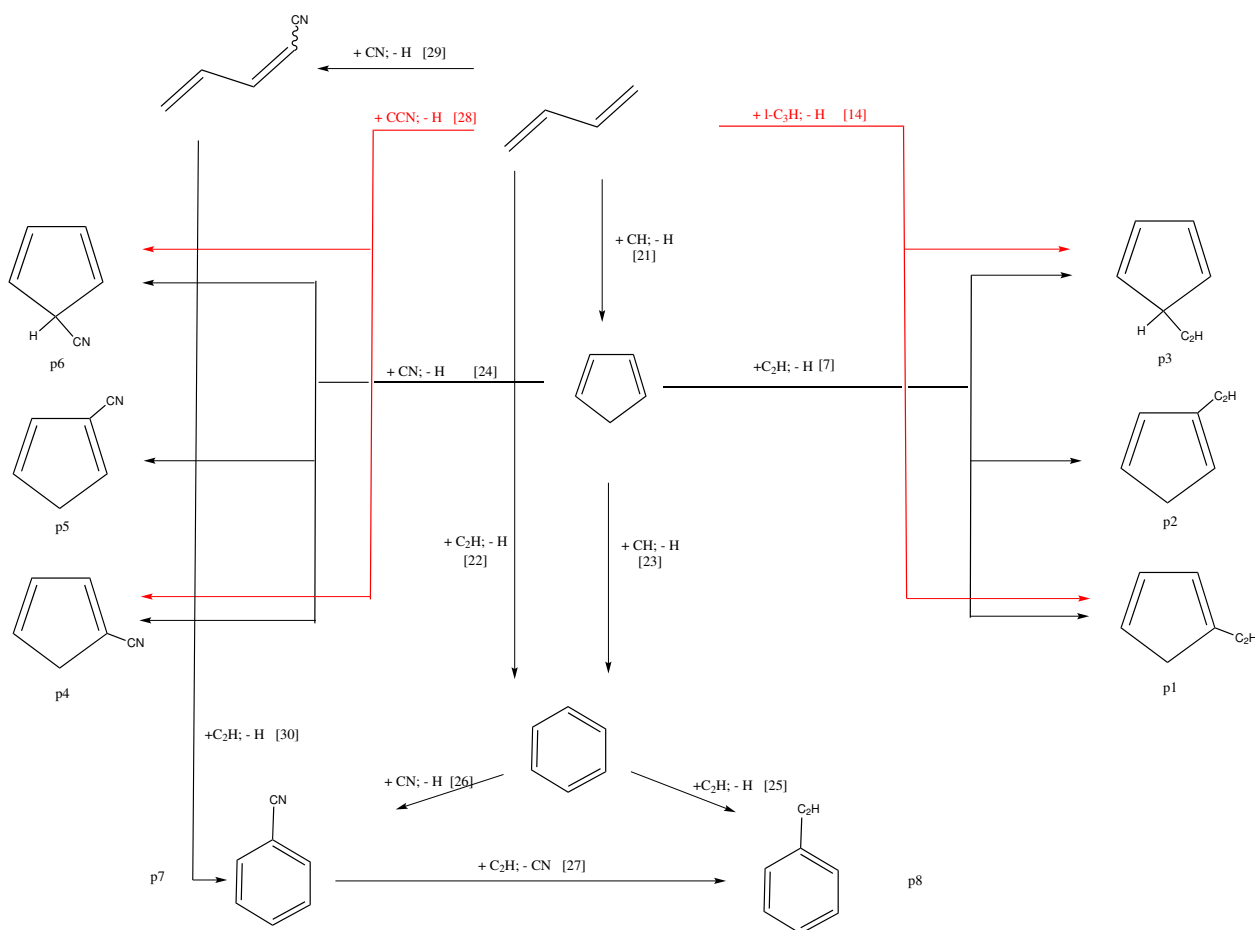


Fig. D.1. Chemical scheme of formation of $c\text{-C}_5\text{H}_6$ and C_6H_6 and their CCH and CN derivatives. Numbers correspond to the reactions discussed in Appendix D.

cyclopropenylidene and vinylidene carbene (H_2CCC) with any doublet C_4H_5 radical are unknown as well. However, considering the molecular structures of the cyclic and carbene-type reactants, formation of 1-*ECP* and 2-*ECP* is unlikely.

Overall, these considerations leave us with reactions [7] and [14] as the most likely pathways to forming 1-*ECP* and 2-*ECP* in TMC-1. Here, reaction [7] represents an addition–hydrogen elimination process that leads to three distinct $\text{C}_5\text{H}_5\text{CCH}$ isomers, $p1$ to $p3$ (see Fig. D.1). Crossed molecular beams merged with electronic structure calculations revealed that reactions of ethynyl radicals with unsaturated hydrocarbons are barrier-less, exoergic, and lead via ethynyl addition to the carbon-carbon triple or double bond followed by hydrogen atom loss to ethynyl-substituted hydrocarbons via molecular mass growth from the bottom up (Jones et al. 2011, and references therein). In the case of vinylacetylene (C_4H_4) and 1,3-butadiene (C_4H_6), the initial addition intermediates isomerize via hydrogen migration and cyclization, leading eventually to *o*-benzyne (C_6H_4) and benzene (C_6H_6), respectively (Fig. D.1; Zhang et al. 2011; Jones et al. 2011). Consequently, the addition of ethynyl to the chemically non-equivalent C_1 and C_2 carbon atoms of cyclopentadiene followed by hydrogen elimination is expected to lead to three distinct $\text{C}_5\text{H}_5\text{CCH}$ isomers, among them the astronomically observed 1-*ECP* and 2-*ECP* ($p1$ and $p2$ in Fig. D.1).

Finally, reaction [14] is worth exploring. Once again, this reaction has not been studied computationally or experimentally. The linear propynylidyne radical (C_3H) is ubiquitous in TMC-1. It can be considered as an ethynyl-substituted methylidyne (CH) radical. Considering that at 10 K methylidyne (CH) reacts with 1,3-butadiene (C_4H_6) to cyclopentadiene (C_5H_6), ethynyl-substituted methylidyne radicals might react to ethynyl-substituted cyclopentadiene isomers $p1$ and $p3$ in barrier-less, overall exoergic bimolecular neutral-neutral reactions (see Fig. D.1).

Overall, reactions [7] and [14] are plausible pathways to forming the ethynyl-substituted cyclopentadiene isomers $p1$ to $p3$ under the conditions present in TMC-1 (Fig. D.1).

Table D.1. Reactions included in the chemical scheme of formation of $c\text{-C}_5\text{H}_6$ and C_6H_6 and their CCH and CN derivatives.

	Reaction	k ($\text{cm}^3 \text{s}^{-1}$)	Comment
21	$\text{CH} + \text{CH}_2\text{CHCHCH}_2 \rightarrow c\text{-C}_5\text{H}_6 + \text{H}$	4.0×10^{-10}	
22	$\text{C}_2\text{H} + \text{CH}_2\text{CHCHCH}_2 \rightarrow \text{C}_6\text{H}_6 + \text{H}$	4.0×10^{-10}	
23	$\text{CH} + c\text{-C}_5\text{H}_6 \rightarrow \text{C}_6\text{H}_6 + \text{H}$	4.0×10^{-10}	
7	$\text{C}_2\text{H} + c\text{-C}_5\text{H}_6 \rightarrow c\text{-C}_5\text{H}_5\text{CCH (1-ECP)} + \text{H}$ $c\text{-C}_5\text{H}_5\text{CCH (2-ECP)} + \text{H}$	1.0×10^{-10} 1.0×10^{-10}	
24	$\text{CN} + c\text{-C}_5\text{H}_6 \rightarrow c\text{-C}_5\text{H}_5\text{CN (1-CCP)} + \text{H}$ $c\text{-C}_5\text{H}_5\text{CN (2-CCP)} + \text{H}$	2.0×10^{-10} 2.0×10^{-10}	
25	$\text{C}_2\text{H} + \text{C}_6\text{H}_6 \rightarrow \text{C}_6\text{H}_5\text{CCH} + \text{H}$	4.2×10^{-10}	Value at 105 K (Goulay & Leone, 2006).
26	$\text{CN} + \text{C}_6\text{H}_6 \rightarrow \text{C}_6\text{H}_5\text{CN} + \text{H}$	5.4×10^{-10}	Value at 15 K (Cooke et al. , 2020).
27	$\text{C}_2\text{H} + \text{C}_6\text{H}_5\text{CN} \rightarrow \text{C}_6\text{H}_5\text{CCH} + \text{CN}$	2.0×10^{-11}	
14	$l\text{-C}_3\text{H} + \text{CH}_2\text{CHCHCH}_2 \rightarrow c\text{-C}_5\text{H}_5\text{CCH (1-ECP)} + \text{H}$	4.0×10^{-10}	
28	$\text{CCN} + \text{CH}_2\text{CHCHCH}_2 \rightarrow c\text{-C}_5\text{H}_5\text{CN (1-CCP)} + \text{H}$	4.0×10^{-10}	
29	$\text{CN} + \text{CH}_2\text{CHCHCH}_2 \rightarrow \text{CH}_2\text{CHCHCHCN} + \text{H}$	4.0×10^{-10}	
30	$\text{CCH} + \text{CH}_2\text{CHCHCHCN} \rightarrow \text{C}_6\text{H}_5\text{CN} + \text{H}$	4.0×10^{-10}	